

**Hydrogen Environment Assisted Cracking of Ultra-high Strength
AetMet™ 100 Steel**

Yongwon Lee and Richard. P. Gangloff

DISTRIBUTION STATEMENT A
Approved for Public Release
Distribution Unlimited

Hydrogen Environment Assisted Cracking of Ultra-high Strength AetMet™ 100 Steel

Yongwon Lee and Richard. P. Gangloff

DISTRIBUTION STATEMENT A
Approved for Public Release
Distribution Unlimited

Abstract

Precipitation hardened martensitic AetMet™ 100 is a high purity ultra-high strength steel with exceptional plain strain fracture toughness ($K_{IC} \sim 130 \text{ MPa}\sqrt{\text{m}}$) and high yield strength ($\sigma_{YS} \sim 1725 \text{ MPa}$). The hydrogen environment assisted cracking (HEAC) behavior of this modern steel is not well understood, and was characterized in neutral 3.5% NaCl solution at various applied potentials (E_{App}) relevant to coated applications in marine environments. A novel short crack specimen was stressed under constant displacement-rate, and monitored using a high resolution electrical potential crack monitoring technique to determine the Stage II crack growth rate (da/dt_{II}) and threshold stress intensity (K_{TH}) typically of the chemically short crack regime (250 to 1000 μm). AerMet™ 100 is susceptible to severe transgranular (TG) HEAC when stressed in neutral 3.5% NaCl and at near free corrosion potentials, as quantified by reduced K_{TH} , to as low as 10% of K_{IC} , and da/dt_{II} as high as 0.5 $\mu\text{m/s}$. Applied electrode potential (E_{App}) is a critical variable. As E_{App} increases from -1.1 volts vs. saturated calomel electrode (V_{SCE}) to $-0.625 V_{SCE}$, operationally defined K_{TH} increases from the very low level of 9 $\text{MPa}\sqrt{\text{m}}$ to a maximum of 40 $\text{MPa}\sqrt{\text{m}}$, and da/dt_{II} decreases monotonically from 500 nm/s to 1 nm/s . Additional polarization to $-0.5 V_{SCE}$, typical of free corrosion in aerated solution, produces a decrease in K_{TH} to 16 $\text{MPa}\sqrt{\text{m}}$ and increase in da/dt_{II} to 100 nm/s . The mechanism for this behavior is crack tip hydrogen embrittlement. The effect of electrode potential is understood based on occluded crack acidification at the anodic conditions and cathodic polarization at lower potentials, each favoring H production and uptake. Scanning electron fractography revealed predominantly transgranular cracking at martensite lath and/or packet interfaces for all applied potentials, caused by enhanced hydrogen localization due to high crack tip stresses and preferential hydrogen trapping. These results are compared to semi-quantitative models for H-enhanced subcritical crack propagation kinetics to identify the rate limiting step, which is likely H diffusion in the crack tip process zone. These results provide the foundation for mitigating HEAC based on electrochemical control of H production/uptake and microstructural control of H trapping/damage. This persisting challenge is to formulate predictive models of this behavior that are useful for engineering design of cracking resistant steels and coatings.

20060710056

I. Introduction

Ultrahigh-strength steels (UHSS) with tempered martensitic microstructures are susceptible to internal hydrogen assisted cracking (IHAC)^[1-4], as well as hydrogen environment assisted cracking (HEAC)^[5-9]. Susceptibility is characterized effectively by the fracture mechanics threshold stress intensity, K_{TH} , below which hydrogen assisted cracking (HAC) is not observed, and rate of subcritical crack growth, da/dt , at stress intensity (K) levels above K_{TH} . The Stage II plateau rate, da/dt_{II} , is approximately independent of K and is characteristic of the rate limiting step in the sequence of time dependent elemental processes that delivers atomic hydrogen (H) to the crack tip fracture process zone (FPZ)^[7]. The mechanism of hydrogen damage is debated between bond-strength reduction and H-plasticity interaction^[5,6,8,10-15].

The severity of HAC is affected by numerous variables that complicate characterization and understanding of steel susceptibility^[7]. A unifying variable is the amount of hydrogen accumulated in the FPZ. This H concentration and damage site location are governed by H trapping at microstructural features, crack tip hydrostatic stress distribution, and source of mobile H^[7]. The FPZ appears to be about 1 μm ahead of the crack tip surface for HEAC in high strength alloys^[17] and at the region of maximum crack tip hydrostatic tension for IHAC^[87]. Traditional UHSS such as AISI 4340 and 300M are particularly susceptible to intergranular (IG) IHAC and HEAC, where impurity segregation at grain boundaries interacts with H to lower boundary cohesion and the associated K_{TH} to a small fraction of the hydrogen-free plane strain fracture toughness, K_{IC} ^[8,13,15]. As a third-important variable, K_{TH} generally decreases and da/dt_{II} increases with increasing tensile yield strength (σ_{YS})^[7,8].

Modern UHSSs such as AerMetTM 100 (UNS K92580) are double-vacuum melted to reduce impurities at prior austenite grain boundaries, and heat treated to produce very high K_{IC} and σ_{YS} ^[19,20]. When cryogenically quenched and optimally aged, AerMetTM 100 is strengthened and toughened by the presence of nano-scale secondary hardening M_2C carbides in unrecrystallized martensite, absence of cementite particles, and formation of a very small amount of thin-film reverted austenite (γ), resulting in K_{IC} of 130 $\text{MPa}\sqrt{\text{m}}$ and σ_{YS} of 1725 MPa ^[21-24]. Despite these advances, AerMetTM 100 is susceptible to HAC comparable to older UHSS^[18,25-30]. For example, IHAC of AerMetTM 100 occurs at a diffusible H concentration, $C_{H,diff}$, as low as 0.5-1 wppm and K_{TH} below 30 $\text{MPa}\sqrt{\text{m}}$. K_{TH} drops to 15 $\text{MPa}\sqrt{\text{m}}$ as $C_{H,diff}$ increases to 8 wppm^[18]. IHAC in AerMetTM 100 is transgranular (TG), attributed to improved austenite

boundary purity, but enabled by H trapping that promotes decohesion of martensite lath and packet interfaces^[18,31,32]. AerMet™ 100 is also susceptible to SCC (that is, HEAC), with K_{TH} varying from 14 to 36 MPa√m for precracked specimens stressed in near-neutral 3.5% NaCl at the freely corroding condition^[26-30]. Fractographic results for HEAC of AerMet™ 100 also vary: one experiment showed a bifurcated IG crack path^[27,28], while others reported predominantly TG cracking^[26,29,30]. Consequently, the hydrogen damage mechanism remains unidentified for AerMet™ 100, particularly the basis for the transgranular crack path.

I.A. Hydrogen Trapping

Hydrogen trapping at microstructural features in UHSS; including carbides of varying coherency, martensite laths and packet interfaces, γ grain boundaries and precipitates, and dislocations^[14,39-42]; can play a dominant role in HAC due to strong influences on the local solubility, C_H , and diffusivity, D_H , of hydrogen. Previous studies of AerMet™ 100 established that nano-scale, coherent and homogeneously dispersed M_2C carbide traps have low H_p -trap binding energies ($E_B \sim 11$ kJ/mol) and are reversible upon stress application, while martensite boundaries have higher binding energies ($E_B \sim 62$ kJ/mol) and are irreversible traps; these features interact to dominate IHAC^[31,32]. Alternatively, Pound argued that irreversible traps dominate HAC and are large, incoherent carbides^[43,44]. These differences in interpretation must be reconciled in order to understand susceptibility to HAC. Moreover, the role of hydrogen trapping depends on the H source and distribution conditions^[45]. Considering IHAC of AerMet™ 100, crack tip stress causes H to re-partition from uniformly distributed M_2C carbide traps to stronger trap sites at interconnected martensite interfaces within the FPZ to cause severe TG cracking^[18,31,32]. In HEAC homogeneously dispersed precipitates may provide a shielding effect by trapping H within the FPZ but away from the crack path. Additionally, trapping will reduce D_H , which is predicted to reduce da/dt_H ^[17]. To test this prediction, precise measurements of crack growth and da/dt_H are needed.

I.B. Effect of Applied Electrode Potential on HEAC of AerMet™ 100

Applied electrode potential, E_{App} , is a particularly important variable for aqueous HEAC because E_{App} controls crack tip overpotential that governs H production and uptake to establish C_H in the FPZ^[7,46,47]. For steels, optimal resistance to HEAC is typically at E_{App} slightly cathodic to the freely corroding range, and resistance decreases for increasing cathodic as well as anodic

polarizations^[47,48]. Steels are typically coated with Zn, Cd or Al to control general corrosion; coating damage will galvanically polarize the exposed steel and potentially degrade HEAC resistance^[49]. On the other hand, galvanic coupling could be tailored by coating composition control to apply a potential that can reduce hydrogen production and thus subcritical cracking. The coating may also dissolve ions that inhibit crack growth by blocking hydrogen uptake at the occluded crack tip^[50,51]. For AerMet™ 100, HEAC behavior in the potential range of -1.100 to -0.400 volts (saturated calomel electrode, V_{SCE}) must be understood to optimize coating design. Dependence of K_{TH} on E_{App} was investigated for AerMet™ 100^[26,30], but results are limited and adversely affected by uncertainties in measured K_{TH} and limited measurements of the effect of applied potential on da/dt_{II} . This potential dependence of HEAC must be better characterized.

I.C. Time Dependence of HEAC and Loading Method

Since H production, uptake and diffusion in the FPZ are time-dependent, K_{TH} and da/dt_{II} are loading rate-dependent, given by dK/dt , and a correct protocol is necessary for accurate characterization of susceptibility^[33,34]. Variances in reported K_{TH} for HEAC likely exist because determination of threshold is challenging despite efforts to standardize the method^[35,36]. Reliable determination of K_{TH} with fixed load or displacement testing may require extremely long test duration (over 10,000 h) since HAC evolves very slowly in steels with low H diffusivity^[17]. Characterizing HAC behavior with shorter duration testing requires a precise crack length monitoring method capable of sub-micrometer resolution, as well as consideration of time dependence. For steels with σ_{YS} above 1000 MPa \sqrt{m} , there is no expected difference between rising K ($dK/dt > 0$) and falling ($dK/dt < 0$) K loading protocols, and either method can be used if executed properly^[7]. However, if the rate of loading exceeds the capability of the rate-limiting step to sustain HEAC, then hydrogen damage will be obscured giving false indication of increased resistance. The commonly used constant displacement protocol^[35] overestimates K_{TH} if the test is terminated before crack arrest occurs or if crack length monitoring is unable to distinguish a slow moving from stationary crack.

A constant load-point displacement rate (rising K) protocol has been used successfully in studies of HEAC of UHSS^[37] and IHAC of AerMet™ 100 in particular^[18], as well as HEAC of high strength Al, Ni and Ti alloys^[7,89]. An applied loading rate of $dK/dt \sim 0.002$ MPa $\sqrt{m/s}$ enables a relatively short (~ 1 day) HEAC experiment. This test method produced severe IHAC in AerMet™ 100; K_{TH} was low and constant until increasing sharply with rising dK/dt only

above $0.3 \text{ MPa}\sqrt{\text{m/s}}^{[18]}$. For HEAC of high strength 4340 steel in purified H_2 , applied-rising dK/dt of $0.001\text{-}0.002 \text{ MPa}\sqrt{\text{m/s}}$ yielded K_{TH} similar to that from long term constant displacement experiments^[36-38]. The effect of dK/dt on K_{TH} for rising load HEAC of AerMet™ 100 has not been established for gaseous or aqueous environments.

I.D. Occluded Crack Electrochemistry and HEAC Test Method Design

The electrochemical conditions at a crack tip in the UHSS-chloride solution system are different from the exposed surface because the crack is occluded^[46,47,52,53]. Important parameters that govern H production and uptake; particularly local pH^[46], potential^[53] and composition of the occluded crack solution^[47]; depend on crack geometry. For example, at anodic potentials oxygen is rapidly depleted by reduction and metal dissolution causes acidification within the crack tip to increase H production and HEAC^[46]. Cathodic potentials promote H production by increasing the hydrogen overpotential for alkaline crack solution and enhance the severity of HEAC^[48]. These processes, and thus K_{TH} and da/dt , could depend on crack geometry^[16].

Accurate electrochemical representation of service conditions requires replication of crack geometry in fracture mechanics specimens. Considering the relatively small critical crack size for an AerMet™ 100 landing gear on the F/A-18E/F fighter^[54], the damage tolerant flaw size range of importance is a $100 \mu\text{m}$ to 3 mm deep surface defect. While a compact tension specimen with a 10 mm crack provides equivalent crack tip stress conditions, a long crack may not reproduce equivalent crack electrochemistry for a short crack^[88]. Experiments established that HEAC for specimens with sub-mm cracks occurs at unexpectedly low K_{TH} values below $10 \text{ MPa}\sqrt{\text{m}}$, as reported for an older steel in chloride solution near free corrosion^[16]. Specimens used in previous studies of HEAC in AerMet™ 100 employed fatigue precrack lengths above $1.7 \text{ mm}^{[25-30]}$. This crack geometry effect must be characterized for modern UHSS. In order to monitor crack length at this scale, the direct current potential difference (dcPD) method was used to continuously measure crack length with $0.5 \mu\text{m}$ resolution^[56].

I.E. Objectives

The objective of this research is to quantify the susceptibility of modern ultra-high strength steel, AerMet™ 100, to HEAC as a function of electrochemical polarization relevant to a coated component in the marine environment. The constant displacement rate method is employed to measure K_{TH} and da/dt_{II} , pertinent to subcritical growth of a chemically short crack.

A second objective is to understand the H-trapping and electrochemical factors that govern K_{TH} and da/dt_{II} . These results provide the basis for coating development as well as assessment of crack tip damage models necessary to predict and optimize the HEAC resistance of modern UHSS.

II. Procedure

II.A. Material and Specimen Design

Forged bar of AerMet™ 100—15 cm in diameter and 1.6 cm thick—was austenitized at 885°C for 1 h, quenched in liquid nitrogen and cold stabilized for 1 h, then aged at 482°C for 5 h and air cooled to obtain the optimal combination of plane strain fracture toughness and strength^[18,21]. The chemical composition and mechanical properties are summarized in Table 1 and 2. The AerMet™ 100 microstructure was characterized by Ayer and Machmeier^[21,24].

Fe	Co	Ni	Cr	Mo	C	Ti	P	S
Bal	13.43	11.08	3.00	1.18	0.23	.009	.003	.0008

HRC	σ_{YS} (MPa)	σ_{UTS} (MPa)	Reduction in Area (pct)	E (GPa)	σ_o (MPa)	K_{IC} (MPa√m)
54	1725	1965	65	194.4	1985	130

Single edge micronotch tensile (SENT) specimens were machined with a width, W , of 10.2 mm and thickness, B , of 2.54 mm. All specimens were machined with the Mode I load applied in the circumferential (C) direction and crack growth in the radial (R) or length (L) direction in the original round-forged bar. C-R and C-L were considered identical because the microstructure of AerMet™ 100 is nearly isotropic. The notch was electrospark discharge machined to a depth of 110 ± 10 μm and mouth opening width of 65 ± 15 μm . To measure crack growth, two platinum wires were spot welded 385 ± 25 μm above and below the notch centerline, across the specimen thickness. The wires were soldered to shielded copper wires that were

affixed to the specimen surface using water resistant epoxy. This specimen and lead wire attachment is detailed elsewhere^[56]. The wired SENT specimen was fatigue precracked to a total notch plus crack depth (a_0) of 200-950 μm in moist air at 10 Hz under constant maximum stress intensity of 11 $\text{MPa}\sqrt{\text{m}}$ and constant stress ratio of 0.10.

II.B. Electrochemical Control and Loading Conditions

Each precracked specimen was loaded in a 340 ml cylindrical Plexiglas cell containing non-deaerated 0.6 M NaCl circulated from a 10 l reservoir at 24 ml/min and room temperature. Solution was not buffered, and periodic measurements of pH confirmed a constant bulk pH of 6.4 for the experiment duration. The gauge length of the specimen was exposed in the solution, precluding solution contact and galvanic coupling with the metal clevis grips. The specimen was configured as the working electrode grounded through the testing machine, while the potentiostat was operated in floating mode to avoid a ground loop. Experiments were run in potentiostatic control with applied potentials ranging from -1.1 to -0.5 V_{SCE} .

The precracked specimen was secured inside the environment chamber with flowing solution, and loaded in a servo-electric feedback controlled tensile machine under constant-slow actuator displacement rate ($d\delta/dt$). The clevis-based gripping configuration allowed free rotation about the loading pins. All specimens were preloaded quickly to 6 $\text{MPa}\sqrt{\text{m}}$, within 30 minutes of specimen polarization, then loaded at a slower test rate. Specimen load, actuator displacement, time, and dcPD data were recorded by automated acquisition.

II.C. Crack Length Measurements Using Direct Current Potential Difference

The dcPD method was used to measure crack length *in-situ*^[55,56]. A constant 10.000 ± 0.005 A direct current source was attached to the specimen grips and voltage-probe wires were connected to a 10,000 gain amplifier. Voltage measurements were unaffected by electrochemical polarization because conflicting ground levels were avoided. The resolution in measured potential was 0.1 μV , which corresponded to a resolvable average crack extension, Δa , of 0.5 μm . A reference specimen was not used to compensate for spurious temperature-dependent dcPD changes because the test duration was relatively short, and additional error can be introduced due to local environmental differences between the active and reference specimens. The slowest reliably distinguishable crack growth rate was 0.2 nm/s.

For every dcPD data point recorded to file, 2,240 potential measurements were taken

over 8.6 s. Thermal voltage contribution to dcPD was eliminated through current reversal where the first 1,120 potentials were measured at an applied current of 10 A, and the latter 1,120 potentials were measured at -10.000 A with a 0.5 s delay to allow for voltage stabilization after current polarity change. The absolute values of these 2,240 voltages were averaged to calculate a single recorded dcPD value that reflected crack length only. This process was triggered every 30 s. The dcPD data were converted to crack lengths by Johnson's equation:^[55]

$$a = \frac{W}{\pi} \cos^{-1} \frac{\cosh\left(\frac{\pi y}{W}\right)}{\cosh\left\{\frac{V}{V_0} \cosh^{-1}\left[\frac{\cosh\left(\frac{\pi y}{W}\right)}{\cos\left(\frac{\pi a_0}{W}\right)}\right]\right\}} \quad [1]$$

where a is crack length, W is specimen width, $2y$ is the distance between lead wire attachments, V is measured potential, V_0 is the dcPD value at a_0 where a_0 is the initial notch depth plus crack length after fatigue precracking, as measured post-fracture. If the final crack length from dcPD did not match within 2% of the actual final crack length, then crack lengths from Eq. 1 were scaled using the following relationship:

$$a_{\text{corrected}} = a_0 + (a_{\text{dcPD}} - a_0) \frac{(a_{\text{final,actual}} - a_0)}{(a_{\text{final,dcPD}} - a_0)} \quad [2]$$

where a_{dcPD} is the crack length calculated from Eq. 1 for a given dcPD value. $a_{\text{final,actual}}$ and $a_{\text{final,dcPD}}$ are measured and calculated values of the final crack length, respectively. Both a_0 and $a_{\text{final,actual}}$ were measured by scanning electron microscopy. A 5 point average of perpendicular distance from the notch front to final crack length was used as actual final crack length. If branching was observed, post-test correction was performed by equating $a_{\text{final,dcPD}}$ to $a_{\text{final,actual}}$, but data collected after the onset of branching were not presented.

II.D. Stress Intensity and Determination of K_{TH}

The following stress intensity solution was used for the SENT specimen with free rotation at the load points^[59]:

$$K = \frac{P\sqrt{\pi a}}{BW} \sqrt{\left[\left(\frac{2W}{\pi a}\right) \tan\left(\frac{\pi a}{2W}\right)\right]} \frac{\left\{0.752 + 2.02\left(\frac{a}{W}\right) + 0.37\left[1 - \sin\left(\frac{\pi a}{2W}\right)^3\right]\right\}}{\cos\left(\frac{\pi a}{2W}\right)} \quad [3]$$

where P is load, B is specimen thickness, W is specimen width and a is crack length.

To define K_{TH} , a plot of P and dcPD values vs load-point displacement, δ , was used (Figure 1)^[58]. First, a probable crack growth initiation point, δ^* , was chosen by visually estimating first deviation in the linear dcPD- δ data (Figure 1b). A baseline was fit by linear regression from $0.7 \delta^*$ to $0.95 \delta^*$, a range selected to eliminate artifacts such as precrack closure in the $0-0.7 \delta^*$ range. A $0.2 \mu\text{V}$ vertical offset was constructed from this baseline. A crack growth line is conventionally fit by linear regression from $1.05 \delta^*$ to $1.3 \delta^*$. However, due to large variance in crack growth behavior among specimens, the growth line fit was based on an assumed initiation dcPD level ($dcPD^*$); with linear regression from $1.01 dcPD^*$ to $1.05 dcPD^*$. K_{TH} was defined operationally as K at the intersection of this growth line and the $0.2 \mu\text{V}$ initiation line offset. To calculate crack growth rate at a given time and K , a 2nd order polynomial was fit to a vs t data over $t \pm 25$ data points. The slope of the tangent at the mid-time point was da/dt and this process was repeated to obtain da/dt at every value of a . Loading rate (dK/dt) was defined in the same manner. The da/dt_{II} is the average da/dt over the Stage-II regime, or reported as a range if growth rate depends mildly on K .

II.E. Fracture Surface Analysis

Fracture surfaces were cleaned ultrasonically in acetone then methanol for 10 minutes, dried, and stored in a desiccator. When necessary, specimens were polarized to $-1.5 V_{SCE}$ in $0.5 \text{ M H}_2\text{SO}_4$ for 60 s or soaked in 10% HCl for 1 ~ 20 minutes to remove corrosion products. A specimen was examined using optical and scanning electron microscopes (SEM). All SEM images are secondary electron images obtained using either 10 kV or 20 kV accelerating voltage. The working distance was varied from 10 mm to 39 mm for optimal conditions. Unless noted, the crack advanced from bottom to top of an SEM or optical image.

III. Results

III.A. K_{TH} and Crack Growth Kinetics Near Free Corrosion

AerMet™ 100 is susceptible to severe HEAC in neutral 3.5% NaCl near the free corrosion potential. Figure 1 is a plot of P and dcPD vs. δ for an SENT specimen tested at $-0.500 V_{SCE}$, maintained constant near the measured open circuit potential of $-0.51 \pm 0.01 V_{SCE}$. From Figure 1b, the operationally defined K_{TH} is $18 \text{ MPa}\sqrt{\text{m}}$, followed by accelerating dcPD and thus subcritical crack growth. Crack initiation is easily detected due to high resolution dcPD crack length monitoring and fast da/dt . The low K_{TH} of $18 \text{ MPa}\sqrt{\text{m}}$ agrees with previously reported threshold values^[26-29], validating the constant extension rate test method for evaluating K_{TH} . Figure 2 shows the stark contrast in crack growth resistance for AerMet™ 100 stressed in 3.5% NaCl compared to moist air^[18], illustrating severe HEAC susceptibility.

Measured subcritical crack growth kinetics are typical of HEAC and reported in Figure 3. The apparent non-zero da/dt below K_{TH} (below 0.2 nm/s) is an experimental artifact related to crack tip blunting, dcPD signal variability, and crack opening effects on dcPD as discussed later. Stage I crack growth behavior is shown clearly; da/dt increases nearly 3 orders of magnitude as K increases from $13 \text{ MPa}\sqrt{\text{m}}$ to $27 \text{ MPa}\sqrt{\text{m}}$. While dK/dt is initially constant with fixed dP/dt ($0.0007 \text{ MPa}\sqrt{\text{m/s}}$), the onset of subcritical crack propagation leads to continuous increase in dK/dt to as high as $0.004 \text{ MPa}\sqrt{\text{m/s}}$. For this loading, a clear Stage-II region is shown with an average da/dt_{II} of 80 nm/s mildly dependent on K . Figure 3 shows that the operationally defined K_{TH} from Figure 1b is greater than the K level at the onset of Stage I growth, in this case $18 \text{ MPa}\sqrt{\text{m}}$ vs. $13 \text{ MPa}\sqrt{\text{m}}$ for loading at $-0.5 V_{SCE}$.

Optical micrographs (Figure 4a-b) show the macro morphology and extent of Mode I HEAC with severe crack branching. The crack branched at K of about $80 \text{ MPa}\sqrt{\text{m}}$ after 1 mm of growth, similar to crack branching reported for a constant displacement, falling K test with AerMet™ 100^[33]. SEM images at crack initiation were compromised due to corrosion, however, fractographs from near the end of the crack (location A in Figure 4a) reveal TG fracture mixed with some evidence of IG growth (Figure 4c and d). This TG crack path is very different from the microvoid-based morphology typical of ductile fracture in AerMet™ 100 at K_{IC} ^[18].

III.B. Effect of Applied Electrode Potential on K_{TH} and Crack Growth Kinetics

Applied electrode potential has a pronounced effect on K_{TH} , as summarized in Figure 5. At the most negative potential of $-1.100 V_{SCE}$, K_{TH} is lowest at $9.3 \text{ MPa}\sqrt{\text{m}}$, which is only 7% of K_{IC} . As potential is raised, K_{TH} increases to a peak value of $41 \text{ MPa}\sqrt{\text{m}}$ (32 % of K_{IC}) at $-0.625 V_{SCE}$ and drops sharply to $18 \text{ MPa}\sqrt{\text{m}}$ (14 % of K_{IC}) at $-0.5 V_{SCE}$. An operationally defined K_{TH} value could not be obtained for the $-0.625 V_{SCE}$ polarization with a $242 \mu\text{m}$ precrack because dcPD signal variability obscured slow-crack growth detection and the maximum K level achievable without significant net-section plastic deformation was $50 \text{ MPa}\sqrt{\text{m}}$. Therefore a specimen with a $947 \mu\text{m}$ precrack was used to expand the linear-elastic loading range to $100 \text{ MPa}\sqrt{\text{m}}$, and a threshold value was obtained following the protocol illustrated in Figure 1. These results establish significant resistance to HEAC at E_{App} of $-0.625 V_{SCE}$ and $-0.700 V_{SCE}$.

HEAC kinetics are highly dependent on applied electrode potential, with Stage-II growth rates varying over 3 orders of magnitude. Figure 6 shows that specimens polarized at E_{App} of $-1.1 V_{SCE}$, $-0.9 V_{SCE}$ and $-0.5 V_{SCE}$ exhibited clearly distinguishable Stage-I and II crack growth regimes. As specimens are loaded above K_{TH} , subcritical crack growth initiates and crack velocity increases rapidly. These crack velocities reached plateaus suggesting approximately K -independent Stage-II growth. Notably, da/dt_{II} decreased from about 500 nm/s to $8\text{-}20 \text{ nm/s}$ as E_{App} changed from $-1.1 V_{SCE}$ to $-0.9 V_{SCE}$, and to as low as $0.5\text{-}2 \text{ nm/s}$ at E_{App} of $-0.7 V_{SCE}$ and $-0.625 V_{SCE}$, before rising to $60\text{-}90 \text{ nm/s}$ at $-0.5 V_{SCE}$. This trend is quantified in Figure 7 using average measured da/dt_{II} represented by the filled symbols. Subcritical cracking over mm-scale distances and severe susceptibility to HEAC are unmistakable for three potentials; $-1.1 V_{SCE}$, $-0.9 V_{SCE}$, and $-0.5 V_{SCE}$.

As shown in Figure 6 and 7, E_{App} of $-0.625 V_{SCE}$ and $-0.7 V_{SCE}$ produced unique behavior with substantially slower da/dt , suggesting high resistance to HEAC. Large increases in K caused only small increases in crack velocity, even when the specimens were loaded beyond the operationally defined level of K_{TH} plotted in Figure 5. For these cases, it is likely that Stage-I behavior exists, but the levels of da/dt are below the 0.2 nm/s noise level inherent in dcPD instrumentation. The behavior observed at $-0.625 V_{SCE}$ and $-0.7 V_{SCE}$ is not complete immunity because subcritical crack growth in fact occurred at these potentials, albeit at very slow growth rates. For example, the specimen polarized to $-0.625 V_{SCE}$ with $a_0 = 242 \mu\text{m}$ showed $28 \mu\text{m}$ of crack growth as it was loaded to $K = 50 \text{ MPa}\sqrt{\text{m}}$ over 20 h. The da/dt_{II} is two orders of

magnitude slower than the level at $-0.5 V_{SCE}$. The sharp increase in da/dt at K of $100 \text{ MPa}\sqrt{\text{m}}$ for the specimen stressed at $-0.625 V_{SCE}$ is likely due to hydrogen enhanced microvoid nucleation at K somewhat below the H-free K_{IC} level of $130 \text{ MPa}\sqrt{\text{m}}$ ^[18].

III.C. Effect of Applied Potential on HEAC Morphology in AerMet™ 100

Fractographic analyses show that HEAC occurred at all electrode potentials examined, but such subcritical cracking was limited to very small increments of growth for E_{App} of $-0.700 V_{SCE}$ and $-0.625 V_{SCE}$, and consistent with Figure 6 and 7. Post-fracture optical images in Figure 8 characterize the macroscopic HEAC front shape as a function of potential. In these low magnification images, specimen thickness is $2,550 \mu\text{m}$ and the notch plus fatigue precrack of about $250 \mu\text{m}$ is barely visible as a bright area at the bottom of each image. The post-test fracture surfaces are shaded and HEAC is darkened in tone from surface roughness and slight corrosion. Parts (a) and (b) show significant crack growth at K below $20 \text{ MPa}\sqrt{\text{m}}$ for the two most negative potentials, while (c) and (d) show no optically resolvable crack growth at $K = 50 \text{ MPa}\sqrt{\text{m}}$ for $E_{App} = -0.7 V_{SCE}$ and $-0.625 V_{SCE}$. The specimen in (e) contained a larger precrack ($947 \mu\text{m}$) and was loaded above K of $100 \text{ MPa}\sqrt{\text{m}}$, but crack growth is not visible. What appears to be a H crack is the fatigue precrack with surface staining. Figure 8f shows substantial HEAC, with the surface covered with black corrosion products produced by polarization at $-0.5 V_{SCE}$.

The effect of potential on HEAC susceptibility is apparent in Figure 8. Test duration for each specimen was approximately 20 h, with the exception at E_{App} of $-1.1 V_{SCE}$, which fractured after 7 h. With identical specimen geometry and loading, E_{App} of $-0.7 V_{SCE}$ produced crack growth of 0.05 mm in 20 h, while the E_{App} of $-1.1 V_{SCE}$ produced 5 mm of HEAC in 7 h. Cracking was similarly limited at $-0.625 V_{SCE}$, but extensive at $-0.5 V_{SCE}$ and $-0.9 V_{SCE}$. Above E_{App} of $-0.7 V_{SCE}$, the final crack front is parallel to the fatigue precrack. However, at E_{App} below $-0.9 V_{SCE}$ the crack front is V shaped (Figure 8a and b). Since all specimens were fatigue precracked to a flat initial crack front, with similar K levels and constraint, the final crack front shape must result from an electrochemical effect on H production and uptake.

High magnification scanning electron microscopy established that HEAC in AerMet™ 100 was predominantly transgranular at all potentials examined, with the exception of cracking near the open circuit potential. This cracking morphology is clearly unique compared to the microvoid fracture mode typical of H-free fracture in moist air^[18], confirming HEAC at each

potential. There was only limited evidence of IG cracking at cathodic applied potentials. An example is shown in Figure 9; HEAC at $-1.1 V_{SCE}$ was completely TG (Figure 9b) and very different from the microvoid morphology typical of fracture in moist air (Figure 9a). Evidence of martensite lath interface cracking is indicated by arrows in Figure 9b, and this path of HEAC is similar to the fractographs obtained for IHAC of this same steel and heat treatment^[18]. This TG HEAC is more complex at other potentials, as illustrated in Figure 4 and 10. At E_{App} of $-0.9 V_{SCE}$, the fracture surface shows predominantly TG cracking (Figure 10a) with localized areas of rough morphology with IG character (triangular arrows in Figure 10a and b). Evidence of martensite lath interface or packet boundary cracking can be found (diamond tipped arrows in Figure 10a and b). Because IG fracture was only suggested on this specimen and not observed at other potentials, the behavior could be due to localized impurity segregation. Alternatively, small deviations in temperature and H concentration can be known to cause a change in the fracture mode for HEAC of UHSS^[9,90]. Diffusible hydrogen concentration of 7.8 wppm caused limited IG cracking in IHAC of this steel^[60].

Two fractographs for E_{App} of $-0.7 V_{SCE}$ and $-0.625 V_{SCE}$ (Figure 10c and e) represent the entire loading range from K of $10 \text{ MPa}\sqrt{\text{m}}$ to $50 \text{ MPa}\sqrt{\text{m}}$. These figures prove that HEAC cracking occurred at both $-0.7 V_{SCE}$ and $-0.625 V_{SCE}$ at growth rates below 1 nm/s with Δa of 50 and $28 \text{ }\mu\text{m}$, respectively, during the 20 h exposure. The fracture surface at $-0.7 V_{SCE}$ is rough (Figure 10d), but the larger features are TG with little resemblance to IG cracking. (Prior austenite grains in this steel are approximately $10\text{--}20 \text{ }\mu\text{m}$ in diameter.) At $-0.625 V_{SCE}$, the crack path is completely TG, ending in a flat area seen in Figure 10e and that could be associated with the limited extent of rapid cracking at high K (Figure 6). For this E_{App} , there is no evidence of IG features (Figure 10e and f). Martensite lath interface cracking was observed at both potentials (diamond tipped arrows in Figure 10c to f). In general, the likelihood of the limited IG-type features coincided with increasing K , crack branching and increased hydrogen production.

III.D. Alternative Method for Measuring K_{TH}

The operational definition of K_{TH} shown in Figure 1b characterizes the stress intensity required to cause the onset of a resolvable amount of HEAC in AerMetTM 100 under rising load-point displacement. At $-1.1 V_{SCE}$ and $-0.5 V_{SCE}$, K_{TH} is easily established because rapid Stage I cracking is readily detected. However, the operational values exceed a true threshold by a significant amount due to the offset method of K_{TH} determination (Figure 1b) and rapid da/dt .

This is illustrated by the interval between 13 MPa√m and the operational K_{TH} of 18 MPa√m, Figure 3. A second error is evident for loading at $-0.7 V_{SCE}$ and $-0.625 V_{SCE}$, where crack growth initiation is masked due to extremely slow Stage I crack growth and Stage II crack growth is below 1 nm/s. The combined SEM images and dcPD data suggest that real crack growth occurred below the operational threshold at these slow cracking potentials and that this operational K_{TH} not an accurate descriptor of a true threshold.

To improve estimation of a threshold for the onset of HEAC and exploit high resolution crack monitoring, an alternative K_{TH}^* was defined as the level of K required to produce measured da/dt of 1 nm/s. This growth rate was chosen because it is the lowest distinguishable rate from the baseline dcPD signal in Figure 6 that can be unambiguously confirmed by SEM images. K_{TH}^* , along with the key results of all experiments, are summarized in Table 3.

Table 3. Summary of HEAC Test Results

E_{App} (V_{SCE})	a_o (μm)	Initial dK/dt (MPa√m/s) [#]	K_{TH} (MPa√m) Figure 5	K_{TH}^* (MPa√m) Figure 6	da/dt_{II} (nm/s) Figure 7	Total Δa (mm)	Termination
-1.100	251	6.1×10^{-4}	9.3	8.3	300-700	~5	Fracture
-0.900	234	7.1×10^{-4}	13.0	10.7	8-20	~4	Branched
-0.700	212	5.5×10^{-4}	24.0	20.1	0.9-2	0.050	Stop/Unload
-0.625	242	5.0×10^{-4}	-	-	-	0.028	Stop/Unload
-0.625	947	11.0×10^{-4}	40.8	22.3	~1	0.1	Stop/Unload
-0.500	250	6.8×10^{-4}	18.0	15.8	60-90	~2	Branched

[#] Applied $d\delta/dt = 12.7$ nm/s for all experiments

IV. Discussion

IV.A. HEAC of AerMet™ 100

The short precrack rising displacement results in Figure 3 and Table 3 establish that optimally aged AerMet™ 100 is susceptible to severe transgranular HEAC in neutral 3.5 % NaCl at free corrosion potentials ($\sim -0.5 V_{SCE}$). The values of K_{TH}^* and K_{TH} are between 16 and 18 MPa√m compared to K_{IC} that is almost an order of magnitude higher. This HEAC behavior is consistent with severe TG IHAC of AerMet™ 100^[18], as well as previous HEAC studies with

AerMet™ 100 using specimens with longer fatigue precracks and various loading methods^[25-30]. Specifically, constant displacement testing showed crack arrest at K_{TH} of 14 MPa√m for 1,000 h total exposure time^[26-28], and constant load testing for 10,000 h resulted in K_{TH} of 16-22 MPa√m^[25,26]. Rising step load experiments yielded K_{TH} of 27 MPa√m^[25,26,30] and a single short-term crack arrest result equated K_{TH} to 14 MPa√m for 20 h exposure^[29]. These test results exhibit substantial variability that bracket the present results, as summarized for E_{App} of $-0.5 V_{SCE}$ in Figure 11. Considering the electrode potential dependence of HEAC in AerMet™ 100, operationally defined K_{TH} values are consistent and perhaps lower compared to previous reports^[25-30] (Figure 11). Compared to rising step-load test results^[25,26,30], this K_{TH} is lower at E_{App} of $-1.1 V_{SCE}$ and $-0.9 V_{SCE}$, essentially equal for $-0.7 V_{SCE}$, and higher for $-0.625 V_{SCE}$. For K_{TH}^* , Figure 11 shows a lower measured threshold compared to existing literature at all tested potentials. Either measure of threshold stress intensity demonstrates that HEAC in AerMet™ 100 is severe at both open circuit potential and below $-0.9 V_{SCE}$, while E_{App} from $-0.625 V_{SCE}$ to $-0.7 V_{SCE}$ provides optimal resistance to HEAC.

Results show that the present accelerated test method, coupled with high resolution crack growth measurement by dcPD, efficiently provides lower bound K_{TH} values (Figure 11) that are relevant to alloy and coating system design, as well as component performance prediction. While all specimens tested were relatively small, the maximum net section tensile stress was below the steel flow strength (1,845 MPa, Table 2), and the plastic zone diameter ($(K/\sigma_{YS})^2/(3\pi) = 160 \mu\text{m}$ at 70 MPa√m) was less than 10% of the remaining ligament, even at the highest K levels and longest crack lengths examined. As such, small scale yielding was guaranteed. Moreover, the small plastic zone diameter to thickness ratio ($< 1-4\%$), lack of resolvable shear walls (Figure 8), and Mode I crack geometry strongly suggest that HEAC was under predominant plane strain deformation. As such, the results in Figure 11 are scalable to large components. The low values of threshold validate the selected dK/dt (~ 0.0007 MPa√m/s in Table 3) as producing K_{TH} that is independent of loading rate. This result is consistent with the loading rate independence of K_{TH} for IHAC in AerMet™ 100 for all $dK/dt < 0.3$ MPa√m/s^[18] and results for gaseous environment HEAC in high strength 4340 steel^[37]. A strong effect of precrack length on K_{TH} is not apparent in Figure 11, particularly given test method and crack resolution differences^[16]. It is reasonable to conclude that these values represent lower bounds on HEAC resistance.

Experimental characterization establishes that improved steel composition and thermal-mechanical processing increased σ_{YS} and K_{IC} for AerMet™ 100, but did not provide immunity to HEAC at any tested E_{App} . This susceptibility of AerMet™ 100 to HAC typified by low K_{TH}^* may limit application of this modern alloy. However, the dramatic decrease in HEAC susceptibility at optimal E_{App} illustrated by greatly reduced da/dt_H is established for the short crack case. This behavior is relevant to small surface cracks in coated UHSS components such as a landing gear.

IV.B. Effect of Steel Composition on Intergranular HEAC

Instances of intergranular HEAC and IHAC in AerMet™ 100 were rarely observed in the present experiments and evidence for this failure mode is limited. Eun reported IG HEAC along interfaces speculated to contain impurities segregated during processing^[28], but such an IG crack growth path was not observed in present experiments or other reports^[26,29,30]. In sharp contrast, older UHSSs such as AISI 4340, 18Ni Maraging and 300M show severe IG HEAC for a wide range of composition, thermal treatment and environmental conditions^[7,8,48]. Impurity segregation to prior austenite grain boundaries is reported to interact with H and cause IG cracking^[8], as characterized by McMahon and coworkers using an impurity-weighted composition parameter ($\psi = Mn + 0.5 Si + S + P$ in weight %)^[8,13,15]. As ψ increases, K_{TH} decreases and the amount of IG cracking increases; immunity to IG HAC is expected for ψ below about 0.05 wt % for steel of $\sigma_{YS} = 1450$ MPa^[15]. While ψ accurately predicts the lack of IG HAC in high purity AerMet™ 100, K_{TH} values measured for TG HEAC (Table 3) and TG IHAC^[18] are far below the values predicted by ψ for this lower strength level of steel. To further investigate the impurity dependence of HEAC of UHSS, high purity 18Ni Maraging and Custom 465™ stainless steels with low Mn and Si were compared to AerMet™ 100). Despite low ψ values of 0.05 to 0.08 wt %, 18Ni Maraging steel and Custom 465™ are susceptible to severe IG HEAC for chloride solution at free corrosion potentials with K_{TH} below 15 MPa \sqrt{m} .

Table 4. Comparison of HEAC and ψ for Commercial High Purity UHSS

	σ_{YS} (MPa)	H-free ψ	Mn (wt %)	Si (wt %)	P (wt %)	S (wt %)	K_{TH} at free corrosion (MPa \sqrt{m})	HEAC Mode
AerMet TM 100	1725	0.029	0.019	0.016	0.001	0.0008	~15	TG
18 Ni Maraging ^[48]	1700	0.045	0.025	0.015	0.008	0.005	~10	IG
Custom 465 ^{TM*}	1600	0.079	0.05	0.04	0.001	0.008	~10	IG

Hydrogen uptake and steel yield strength affect this ψ correlation, as recognized by McMahon et al.^[8,15]. For a high purity (Mn and Si free) steel, K_{TH} decreased from 95 MPa \sqrt{m} to 35 MPa \sqrt{m} with increasing yield strength from 1450 MPa to 1860 MPa and increasing H_2 pressure, presumably associated with increasing intergranular cracking. These additional effects were well described by a revised composition parameter that included an estimate of crack tip H content, $\psi = 10^4 C_{H-S} + Mn + 0.5 Si + S + P$, with immunity suggested for ψ below 0.7 atom %^[8,15]. Here, C_{H-S} was calculated from Sievert's law for gaseous exposure, increased to account for crack tip stress but not considering trapping. The multiplier of 10^4 was necessary to fit the H concentration effect with that of the other elements. While the Maraging and Custom 465TM steels are relatively pure, the H concentration from NaCl may be sufficiently high to align K_{TH} results with this H-containing ψ correlation for IG cracking in H_2 . Compared to AerMetTM 100, prominent IG cracking may be due to somewhat higher S, Mn and Si contents in the Maraging and Custom 465 steels, and hence slightly higher H-modified ψ (Table 4), but this is speculative since austenite grain boundary compositions were not measured. While it is uncertain whether lower purity AerMetTM 100 will display IG HEAC and IHAC, these comparisons show that grain boundary purity is not the single critical factor that governs HAC immunity in modern and relatively pure UHSS. As developed in an ensuing section, very high levels of H can be trapped at austenite and martensite boundaries in UHSS, enhanced by very high crack tip stress and high trap binding energy. K_{TH} is controlled by this localized H, coupled with the intrinsic boundary strength and reduction due to H decohesion. The H-modified ψ suggested by McMahon and

* In collaboration with Kehler and Scully, 2 cm diameter round bar of Custom 465TM was aged for 4 h at 482°C and air cooled to obtain $\sigma_{YS} = 1600$ MPa^[91]. Specimens were machined and tested with identical loading and electrochemical conditions outlined for AerMetTM 100. HEAC of Custom 465TM was IG with K_{TH} below 12 MPa \sqrt{m} at all tested E_{App} of -1.100, -0.625, -0.575, and -0.500 V_{SCB}^[91].

coworkers^[8,15] is aligned with this explanation, but is not sufficiently quantitative.

IV.C. Effect of Applied Potential

Applied electrode potential strongly affects the kinetics of HEAC in AerMet™ 100, as shown by the results in Figures 6, 7 and 11. Pioneering work by Brown qualitatively demonstrated the effect of E_{App} on da/dt , with the slowest crack growth rates for older UHSSs in the applied potential range of $-0.8 V_{SCE}$ to $-0.9 V_{SCE}$ and increased cracking at more anodic and more cathodic potentials^[47]. Similar effects were noted for HEAC of 18Ni Maraging steel, with optimal cracking resistance at an applied potential $\sim 0.2 V$ cathodic of free corrosion^[48]. AerMet™ 100 parallels this potential dependence (Figure 11), with the highest K_{TH} and lowest da/dt_{II} values when polarized to $-0.7 V_{SCE}$ and $-0.625 V_{SCE}$, or slightly cathodic with regard to the open circuit potential of $-0.51 V_{SCE}$.

The potential dependence of HEAC is explained based on changes in the concentration of lattice-dissolved H (C_L), in equilibrium with crack tip pH and potential. The electrochemical principles that govern C_L vs. E_{App} are well established^[7,47,52,61,62] and modeling approaches for idealized-quantitative prediction have been developed^[16,46,63]. It is not, however, possible to accurately predict absolute values of C_L , K_{TH}^* , and da/dt_{II} vs. E_{App} ^[7]. The trend in these properties is predicted based on a minimum in the overpotential for crack tip H production. Specifically, H overpotential and C_L are large, with associated low K_{TH}^* and high da/dt_{II} for two regimes of applied potential. When crack tip corrosion occurs near free corrosion, local pH is lowered relative to the bulk-neutral chloride solution via hydrolytic acidification of Fe and Cr, to increase overpotential at the crack tip relative to the boldly exposed surface. At the other extreme, substantial and increasing cathodic polarization promotes increasingly high H overpotential and thus increased C_L . The maximum in K_{TH}^* and minimum in da/dt_{II} are produced in the range of E_{App} where crack tip dissolution and acidification are reduced to near 0 and crack tip cathodic polarization is minimal, producing minimal overpotential and minimal C_L .[†] Quantitative coupling of this E_{App} dependence of C_L with K_{TH}^* and da/dt_{II} is considered in

[†] Crack front shape exhibited significant differences due to applied potential change, as shown in Figure 8. This behavior is consistent with the fact that crack tip cathodic polarization is somewhat less than that at bold surfaces due to crack potential difference and crack pH increase. At anodic potentials, the crack advances as a flat front without preferential propagation at the side surface because H overpotential is much larger within the crack compared to the boldly exposed surfaces.

the ensuing section on micromechanical modeling of FPZ H embrittlement.

IV.D. Stress and Trapping Enhanced H Localization

The severity of transgranular HEAC in a high purity UHSS such as AerMet™ 100 is understood based on significant crack tip microstructural trapping and stress enhancement of C_L . This enhanced H concentration, $C_{H\sigma,T}$, is approximated by:^[7,84,93]

$$C_{H\sigma,T} = C_L \exp\left(\frac{E_B}{RT}\right) \cdot \exp\left(\frac{\sigma_H V_H}{RT}\right) \quad [4]$$

where V_H is the partial molar volume of H in the lattice (2.0 cm³/mol), σ_H is crack tip hydrostatic stress, E_B is the binding energy of H to a specific trap site, R the universal gas constant and T is temperature. Equation 4 is accurate for the situation where $C_{H\sigma,T} \ll 100$ atom percent. For a given value of C_L , the equilibrium concentration of hydrogen at interconnected microstructural sites that constitute the crack path is determined by the stress field interaction energy ($\sigma_H V_H$) plus E_B , assuming that σ_H does not affect E_B . While C_L is typically low, of order 0.0005 wppm for a H overpotential of 0^[14,18,62], $C_{H\sigma,T}/C_L$ is high for a high purity UHSS and it is this enhancement that drives HEAC. Crack tip σ_H is 3 to 10 times σ_{YS} due to various crack tip shielding mechanisms as modeled by traditional plasticity considerations, dislocation mechanics or strain gradient continuum plasticity^[7,64-66]. For a reasonable crack tip hydrostatic stress of $5\sigma_{YS}$, $\sigma_H V_H$ is ~17.5 kJ/mol for AerMet™100, yielding $C_{H\sigma,T}/C_L$ of 1,200 from Eq. 4. Fractographic results in Figure 9 and 10 show brittle TG features consistent with cracking along martensite lath interfaces and packet boundaries. A very large concentration of H accumulates along these incoherent interfaces due to preferential trapping. The binding energy for H to such trap sites is about 60 kJ/mol^[31,32]; from Eq. 4, $C_{H\sigma,T}/C_L = 6 \times 10^6$ for a lower bound of this binding energy (40 kJ/mole) coupled with $\sigma_H V_H$ of ~17.5 kJ/mol. For the zero overpotential estimate of C_L , the maximum value of $C_{H\sigma,T}$ enriched along martensite interfaces is 1,600 wppm (9 atom pct). This hydrogen enrichment provides ample cause for interface weakening by the decohesion mechanism and thus the path for HEAC, consistent with results for IHAC of AerMet™ 100^[18]. Crack tip electrochemical conditions that cause a finite H overpotential will increase this level of FPZ H to lower K_{TH} , while surface reaction rate and H diffusion rate limitations will reduce da/dt_{II}

The lack of prior austenite boundary cracking in HEAC or IHAC is not explained by increased grain boundary purity because the binding energy of H to incoherent grain boundaries typically exceeds 50 kJ/mol^[32], and such interfaces should trap H analogous to the case for martensite lath and packet boundaries. Such a high $C_{H\sigma,T}$ should embrittle prior austenite grain boundaries in the absence of co-segregated impurities. The fact that IG cracking is observed in a wide range of UHSSs negates the argument that there is a small probability that large (10-20 μm) prior austenite grain boundaries intersect the sub- μm FPZ compared to martensite lath and packets sized from 0.5 μm to 5 μm . The alternate hypothesis is that the intrinsic fracture strength of segregation-free prior austenite boundaries exceeds that of certain martensite interfaces for equal or even greater concentrations of trapped H.

Thin-film austenite that precipitates between martensite laths could provide an explanation for a preferred martensite interface crack path in both IHAC^[18] and HEAC of AerMetTM100. This phase, which forms during aging, likely enhances $C_{H\sigma,T}$ through trapping and solubility considerations. Moreover, elevated stresses in the FPZ could cause thin-film γ' to transform to martensite of higher volume ahead of the crack tip^[67,68]. If this fcc austenite is enriched with H, the martensite will be supersaturated causing a transient increase in interlath hydrogen concentration which will further enhance interface cracking. Conversely, Ritchie *et al.* showed that retained interlath austenite is mechanically stable when present as a continuous network, and enhances intergranular cracking resistance by attracting impurities and impeding H diffusion^[69]. Olson argued that a thin austenite film is stabilized because the number of martensite nucleation sites is small and partitioned alloy content is high^[70]. Nohara's composition correlation for stainless steels (which does not consider Co) shows that the deformation induced martensite transformation temperature (M_D) of γ' in AerMetTM 100 is far below 0 K ($M_D = -390\text{ }^\circ\text{C}$)^[71]. This stability is countered by the fact that dissolved H promotes γ transformation to martensite^[72,73]. The relative importance of these competing mechanisms is unclear for γ' in AerMetTM100.

Hydrogen traps play a complex role in both IHAC and HEAC of high strength alloys^[7,14,39,44,74]. In HEAC consideration of H diffusion suggests that H damage is localized to within 1 μm from the crack tip surface^[7,17]. The dcPD measurements of HEAC in AerMetTM 100 stressed in NaCl did not evidence discontinuous crack advance at the 1 μm resolution level, consistent with this small FPZ distance. For a prior austenite grain size of 10~20 μm , a 1 μm

FPZ contains a small fraction of γ grain boundaries and coarse carbides, a somewhat higher density of martensite boundaries, but a very dense population of homogeneously distributed M_2C precipitates. M_2C traps within the FPZ could shield the FPZ from hydrogen damage by trapping H preferentially away from the martensite interfaces. A homogeneously dispersed fine carbide phase will only act as a beneficial shielding trap in HEAC if: (a) E_B is substantially higher than E_B for crack path trapping,[†] and (b) trapping at fine particles is not saturated by the high level of C_L and finite number of carbides in the FPZ. These conditions were not realized for peak aged AerMet™ 100, and low K_{TH}^* for TG HEAC were produced at both cathodic and anodic potentials. Speculatively, the M_2C phase could be coarsened to reduce coherence and increase E_B to induce H shielding, for example through higher temperature aging or Cr addition^[21,23,24]. Such shielding may be particularly exploited at E_{App} between -0.625 and -0.700 V_{SCE} where the absorbed hydrogen concentration is reduced by lower crack tip driving force for H production. While K_{TH} is controlled by equilibrium C_L , da/dt_{II} may be limited by H diffusion or surface reaction rate control. When the latter is important, the likelihood of carbide trap saturation is reduced and the relative beneficial effect of such shielding should be enhanced. In the least, interaction with M_2C results in reduced H diffusivity and thus reduced da/dt_{II} as developed in the next section.

IV.E. HEAC Propagation Kinetics

HEAC propagation kinetics are understood based on the concept of a rate limiting step in the overall sequence of H production on the crack surface and delivery to the FPZ^[7,9,92]. Surface reaction controls da/dt_{II} if the rates of H production, migration, adsorption or absorption are slower than the rate of H diffusion from the sub-surface to the FPZ. Weakly aggressive environments or coated surfaces which block H permeation are representative cases of surface reaction limited growth, in which trap enhanced H concentration under the exposed crack tip surface, C_s , changes with time. For more aggressive environments, C_s reaches an equilibrium level quickly and H diffusion controls da/dt_{II} ^[63]. A one dimension model, solved with a variety of boundary conditions, yields a prediction for da/dt_{II} of the form^[17]:

[†] Based on relative trap binding energies, $E_B = 11$ kJ/mole for coherent M_2C and 40-60 kJ/mol for incoherent martensite interfaces^[32], the probability that H partitions to the martensite from M_2C is near unity^[75,76].

$$da/dt_{II} = \frac{D_H}{X_C} \left[\xi \left(\frac{C_S}{C_C}, D_H, X_C, \sigma_{YS}, t \right) \right] \quad [5]$$

where t is time, X_C is a critical distance ahead of the crack tip surface, C_C is a critical H concentration necessary for damage, and ξ is a functional description of the driving force for H ingress that depends on the assumed boundary conditions^[17,77,78,80-82,93]. The C_C depends on local stress. In this modeling, the crack is hypothesized to propagate when C_C is reached at X_C such that:

$$\frac{da}{dt_{II}} = \frac{X_C}{\Delta t} \quad [6]$$

where Δt is the time required for the hydrogen concentration to reach C_C at locations on average X_C within the FPZ.

Figure 7 shows that E_{App} strongly affects da/dt_{II} for HEAC in AerMetTM100, with a minimum produced by cathodic polarization from free corrosion through $-0.7 V_{SCE}$, followed by increasing da/dt_{II} to $0.7 \mu\text{m/s}$ at $-1.1 V_{SCE}$. The electrochemical driving force for H production is very high at this potential and HEAC can be presumed to be diffusion limited. This expectation is supported by an empirical correlation between upper bound plateau crack growth rates for a wide variety of high strength alloys, plotted in Figure 12 vs. trap sensitive H diffusivity, D_H ^[17]. The linear dependence of da/dt_{II} on D_H is confirmed for situations involving very severe environments, including AerMetTM100 under severe cathodic polarization ($-1.1 V_{SCE}$) and presumably high levels of C_S that are established rapidly resulting in diffusion limited HEAC. For this upper bound correlation, and an assumed value of the ξ function equal to 3, the data in Figure 12 suggest that $X_C = 0.7 \mu\text{m}$. It is important to determine the extent to which the diffusion based modeling, Eqs. 5 and 6, can predict the electrode potential dependence of da/dt_{II} shown in Figure. 7. Kehler et al. used the measured E_{App} dependence of K_{TH} shown in Figure 5 with the constants shown in Table 5 to predict the E_{App} dependence of C_S for AerMetTM 100 in NaCl solution^[50]. This is the local H concentration in the FPZ and in equilibrium with a given applied potential, and crack tip H overpotential. This crack surface concentration boundary condition is a critical element of crack growth rate analysis, and the use of reverse engineering from a threshold-based model is a valid starting point for da/dt_{II} modeling, as demonstrated by Symon and Hall for HEAC of nickel-based superalloys^[82,93]. This kinetics modeling will be complicated by the likelihood that: (a) D_H depends on hydrogen concentration and trap density, (b) the

binding energies of trap states associated with the critically important martensite lath and packet interfaces are not sufficiently quantified^[32], and (c) the critical distance developed from the correlation shown in Figure 12 may vary with E_{App} and thus C_S . Additionally, C_S may not be at equilibrium with the crack tip H overpotential in the time frame of crack advance; as such, da/dt_{II} would not be strictly H diffusion limited as required for Eq. 5 to be valid^[63]. This detailed analysis of crack growth kinetics is the subject of proposed research in the next phase of this project^[94].

The engineering significance of da/dt_{II} is especially pronounced when da/dt_{II} is slow, as it is at $-0.625 V_{SCE}$ and $-0.7 V_{SCE}$ in Figure 7. For example if a component is polarized to $-0.625 V_{SCE}$, it would take 70 days of continuous loading at $50 \text{ MPa}\sqrt{\text{m}}$ in 3.5% NaCl to grow the critical crack size of 6 mm prescribed for an AerMetTM100 landing gear^[54]. This is of critical importance, because the same loading conditions at $-0.5 V_{SCE}$ would grow the same crack length in 20 h; at $-1.1 V_{SCE}$ it would take less than 4 h. Although the experimental results in this work show that perfect immunity is not obtained at any potential, polarization at $-0.7 V_{SCE}$ to $-0.625 V_{SCE}$ can significantly prolong component lifetime and reduce inspection frequency. This regime of applied potential is ideally suited for coupling with H production or uptake inhibitors, or microstructural alteration of H trap states, as the foundation for mitigating HEAC of UHSS.

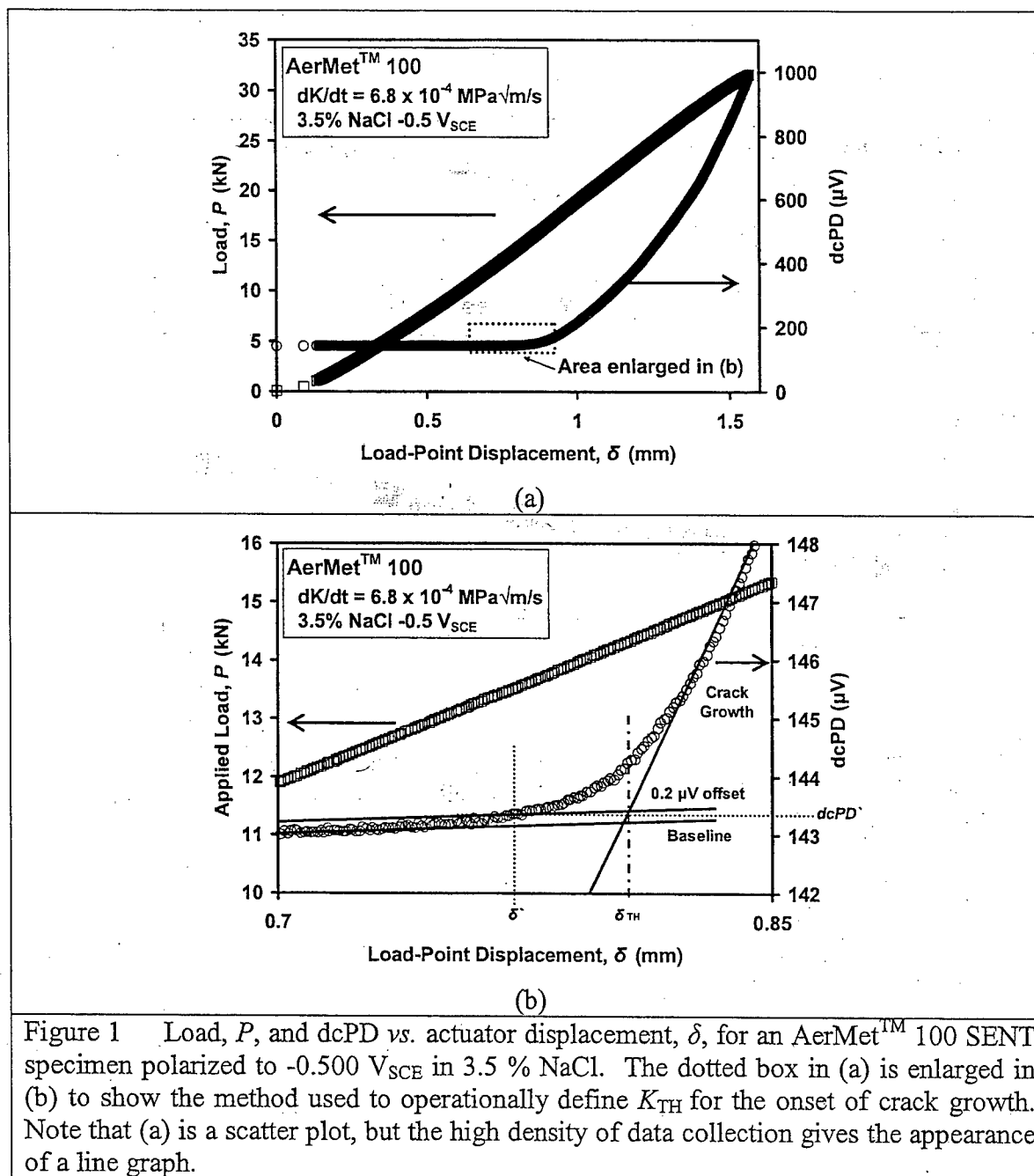
V. Conclusions

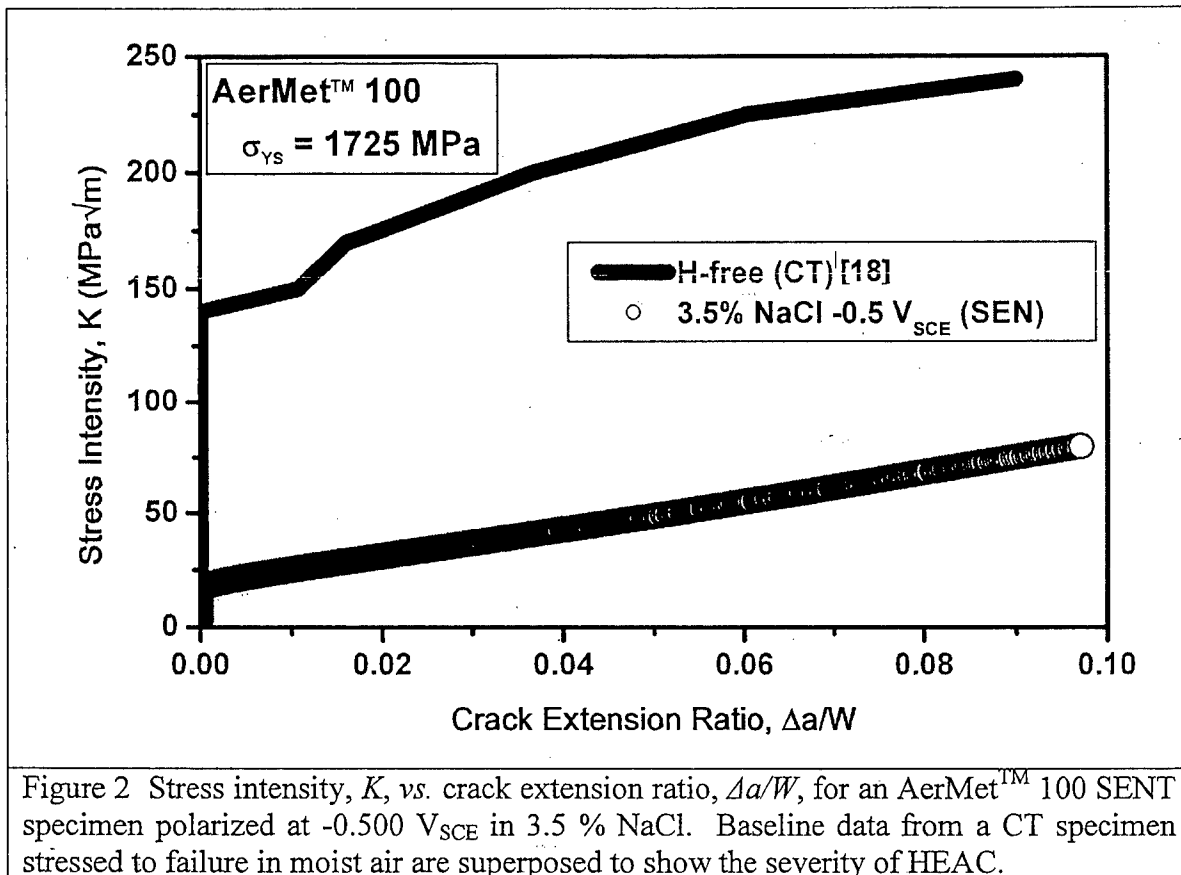
1. AerMetTM 100 is susceptible to severe transgranular hydrogen environment assisted cracking (HEAC) when stressed under slow-rising displacement in neutral 3.5% NaCl and at near free corrosion potentials, as quantified by two parameters: reduced threshold stress-intensity for HEAC, K_{TH} , to as low as 10% of K_{IC} , and subcritical crack growth rate, da/dt , as high as hydrogen diffusion rate limited values on the order of $0.5 \mu\text{m/s}$.
2. The slow-rising load method with high-precision dcPD monitoring of crack growth provides an accurate and accelerated characterization of the operationally defined threshold-onset of HEAC for da/dt above 1-2 nm/s. The true threshold and Stage I growth kinetics are ambiguous for cases where da/dt is less than this level.
3. Short crack size does not dramatically promote HEAC of AerMetTM 100 in NaCl compared

to more conventional measurements of K_{TH} and da/dt based on fracture mechanics specimens with long cracks.

4. High binding energy traps, in particular martensite lath/packet boundaries form the transgranular crack path of HEAC in AerMet™ 100.
5. The improved purity of AerMet™ 100, in particular reduced S and P as well as Mn and Si contents, does not provide immunity to HEAC or substantially increase K_{TH} . However, the increased purity may increase the inherent grain boundary strength leading to the absence of intergranular cracking.
6. The HEAC susceptibility of AerMet™ 100 is strongly dependent on applied potential. Severe HEAC, with low K_{TH} and high da/dt_{II} , is produced at potentials that are substantially cathodic, as well as at or mildly anodic with regard to the free corrosion potential regime for aerated sodium chloride solution.
7. An electrode potential range exists at slightly cathodic potentials between -0.625 and -0.700 V_{SCE} , where HEAC susceptibility is greatly reduced, particularly as characterized by reduced crack growth rates. However, complete immunity to HEAC is not obtained at any applied potential.
8. The applied potential dependence of K_{TH} and the crack front shape agree with electrochemical considerations for an occluded crack tip in chloride solution, including increased H production from crack acidification at anodic potentials and crack polarization at cathodic potentials.
9. A semi-quantitative analysis of da/dt_{II} shows that HEAC is likely to be H-diffusion limited at potentials that are substantially cathodic, as well as at or mildly anodic, with regard to the free corrosion potential regime for aerated sodium chloride solution. Significant uncertainties exist and preclude mechanism based modeling of the electrode potential dependence of da/dt_{II} .

Figures





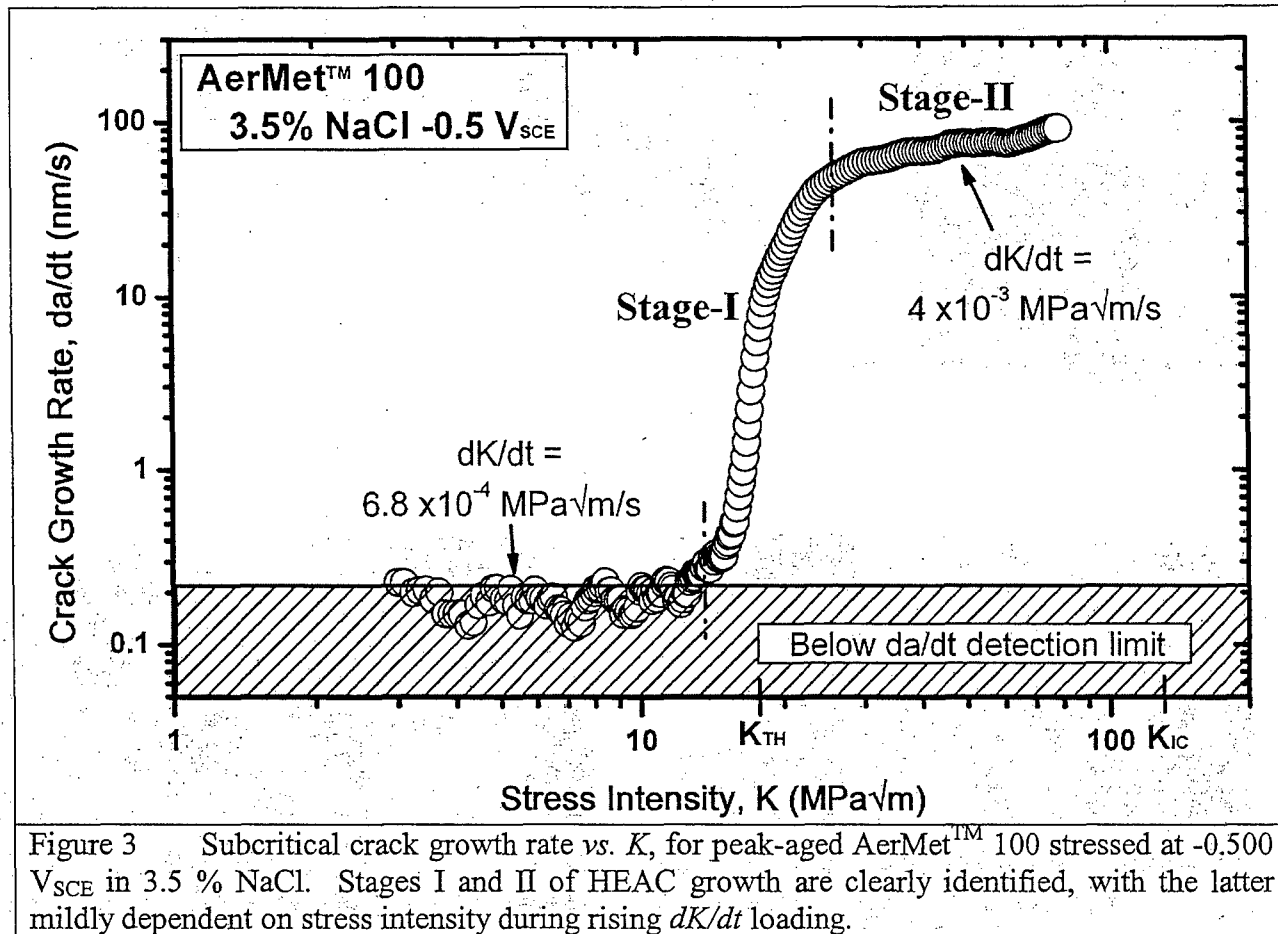


Figure 3 Subcritical crack growth rate vs. K , for peak-aged AerMetTM 100 stressed at $-0.500 V_{SCE}$ in 3.5 % NaCl. Stages I and II of HEAC growth are clearly identified, with the latter mildly dependent on stress intensity during rising dK/dt loading.

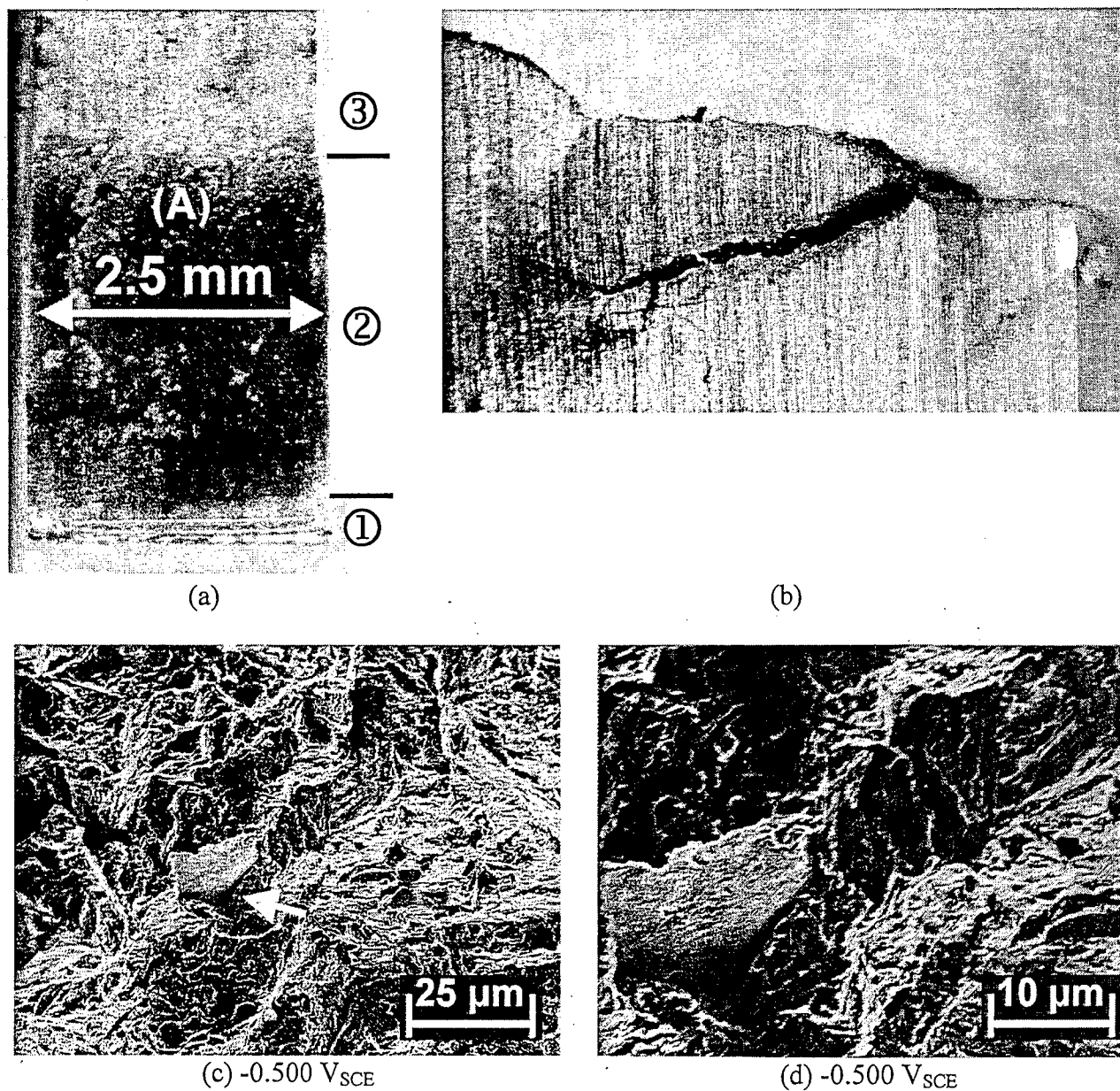


Figure 4 Optical and scanning electron images of an AerMet™100 specimen tested in 3.5% NaCl at $-0.5 V_{SCE}$. (a) ① = notch and fatigue precrack, ② = HEAC and ③ = fracture in air. (b) The side profile shows the extent of branching, with HEAC occurring from right to left. At the location of branch; average crack length is about 1 mm and approximate stress intensity is $75 \text{ MPa}\sqrt{\text{m}}$. The SEM images (c) and (d) are taken from location (A), and shows TG fracture mixed with some IG fracture (arrow).

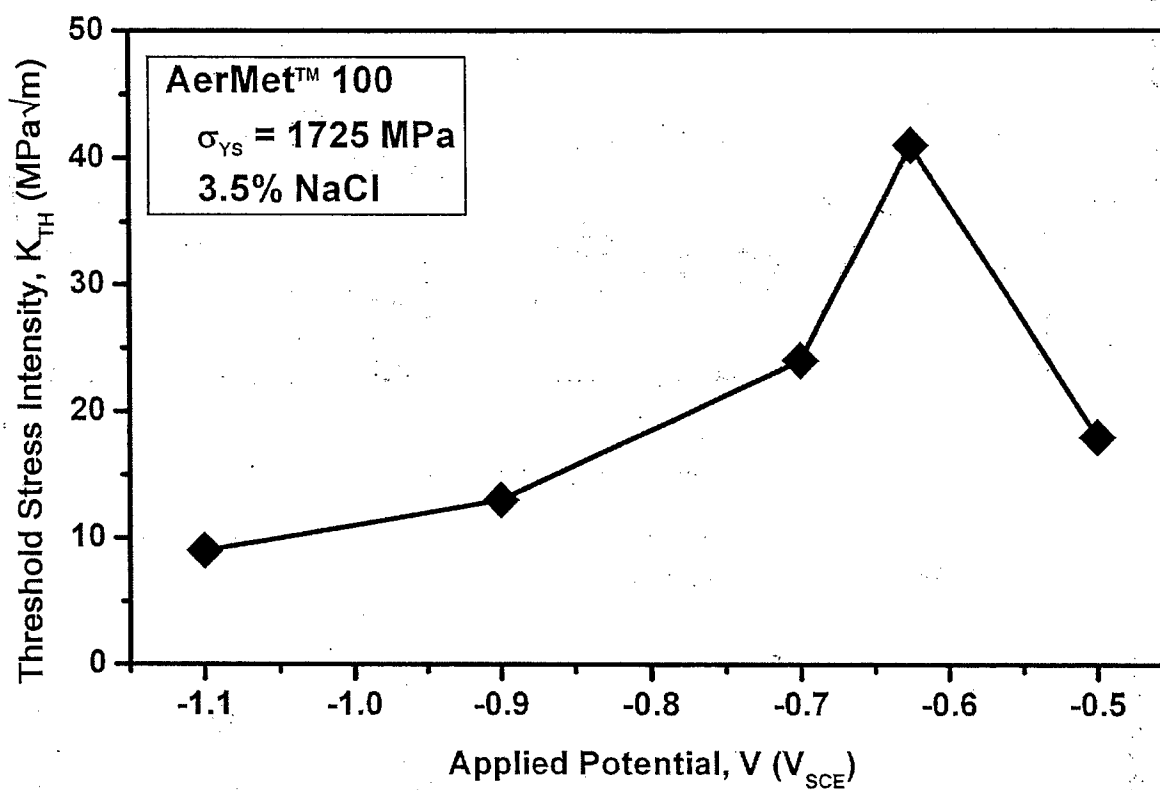
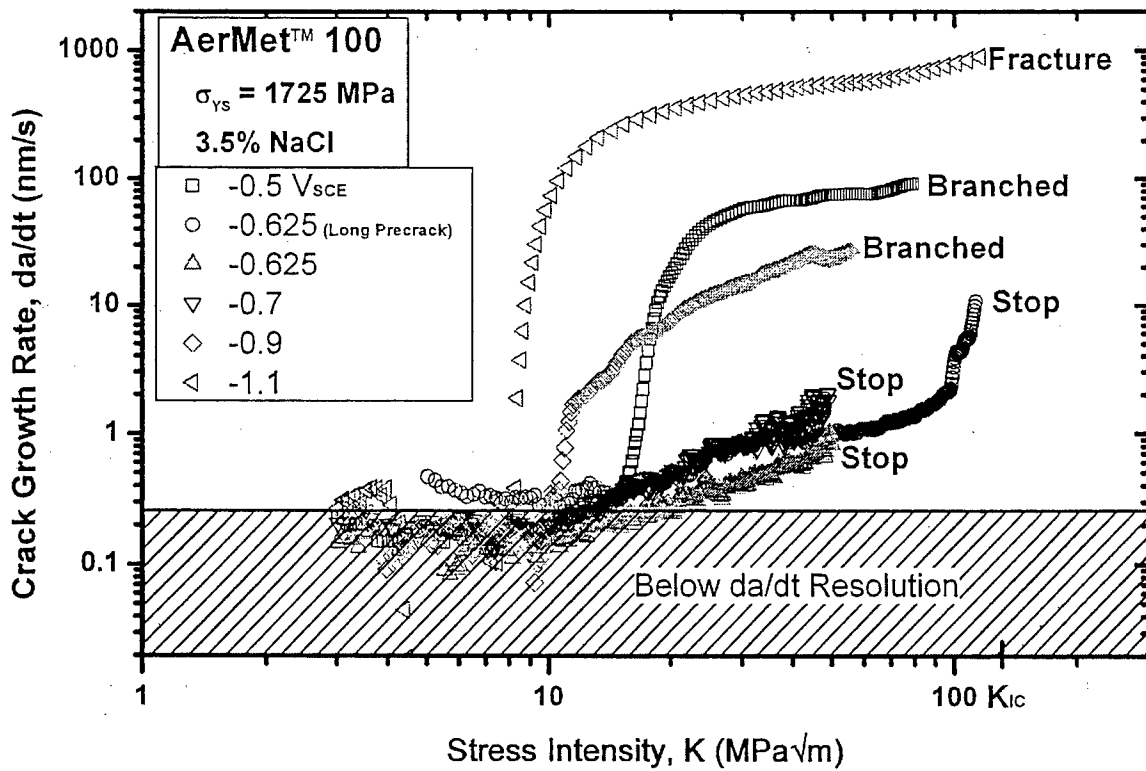
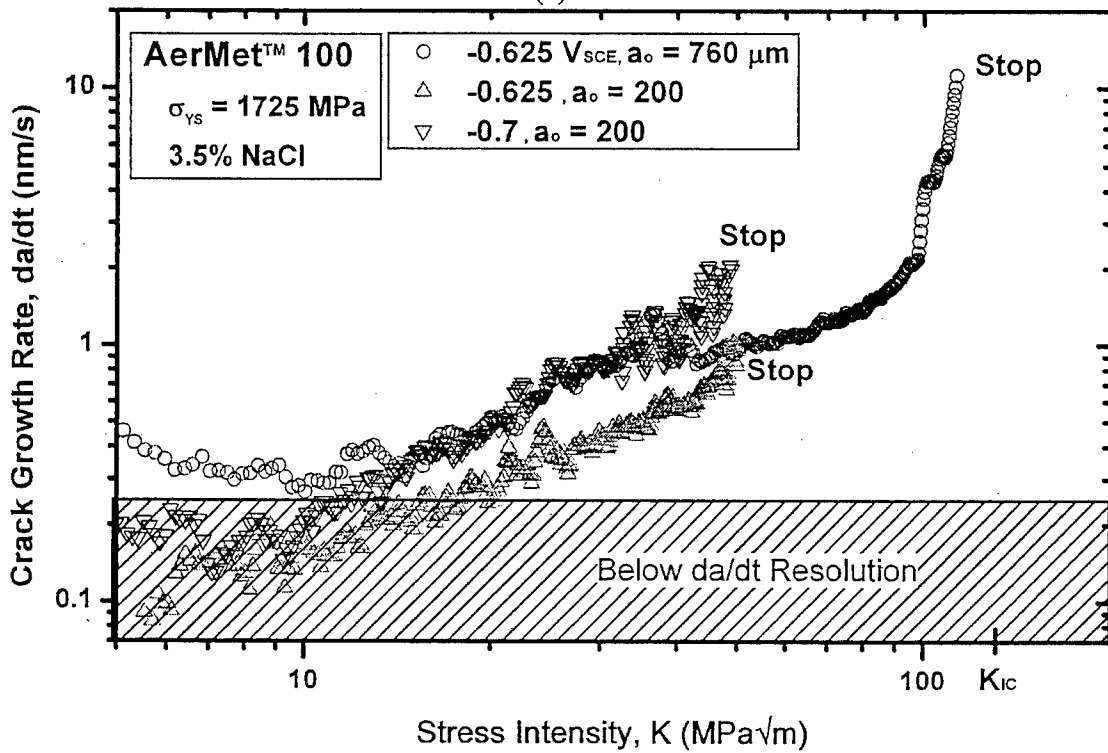


Figure 5 Threshold stress intensity, K_{TH} , vs. applied potential for peak-aged AerMet™100 stressed at constant $dK/dt = 6 \times 10^{-4}$ MPa√m/s in 3.5 % NaCl.



(a)



(b)

Figure 6 Crack growth rate vs. stress intensity for peak-aged AerMet™100 in 3.5 % NaCl.

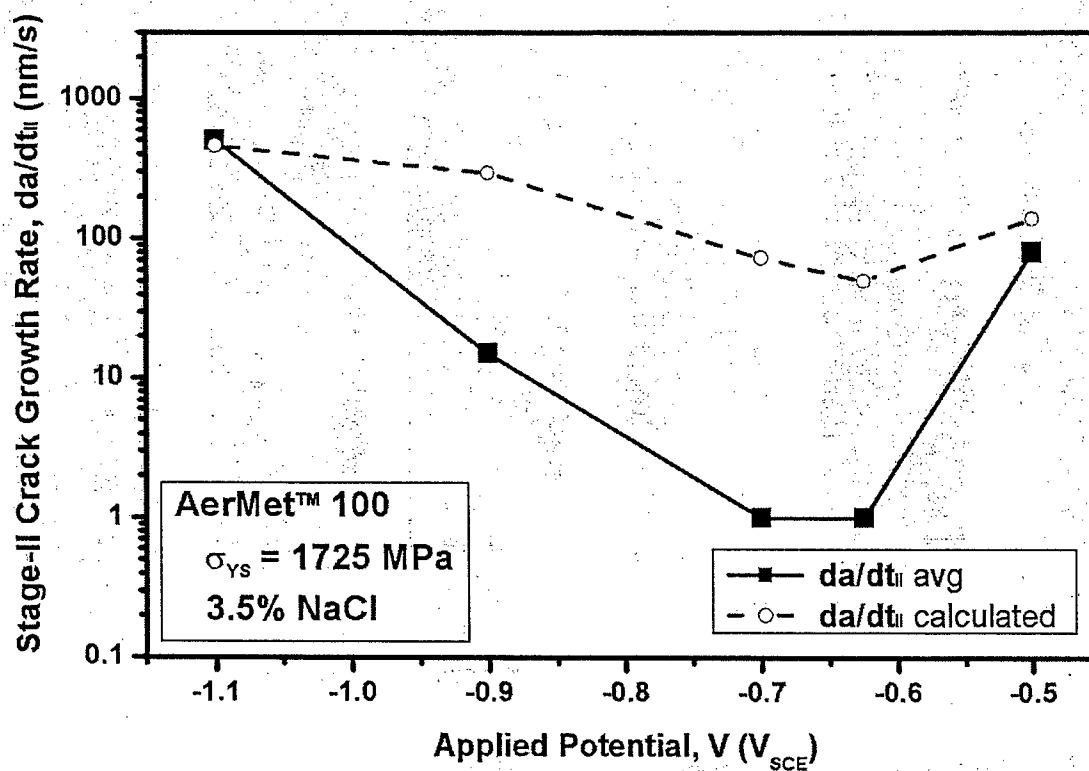


Figure 7 Stage-II crack growth rate, da/dt_{II} , vs. applied potential for peak-aged AerMet™ 100 in 3.5 % NaCl. da/dt_{II} is an average value obtained from Table 3 and is substantially slower at $-0.700 V_{SCE}$ and $-0.625 V_{SCE}$. The calculated da/dt_{II} for H diffusion limited controlled crack growth is based on simple application of Eq. 5 coupled with data on the applied potential dependence of C_S from Kehler et al.^[50]

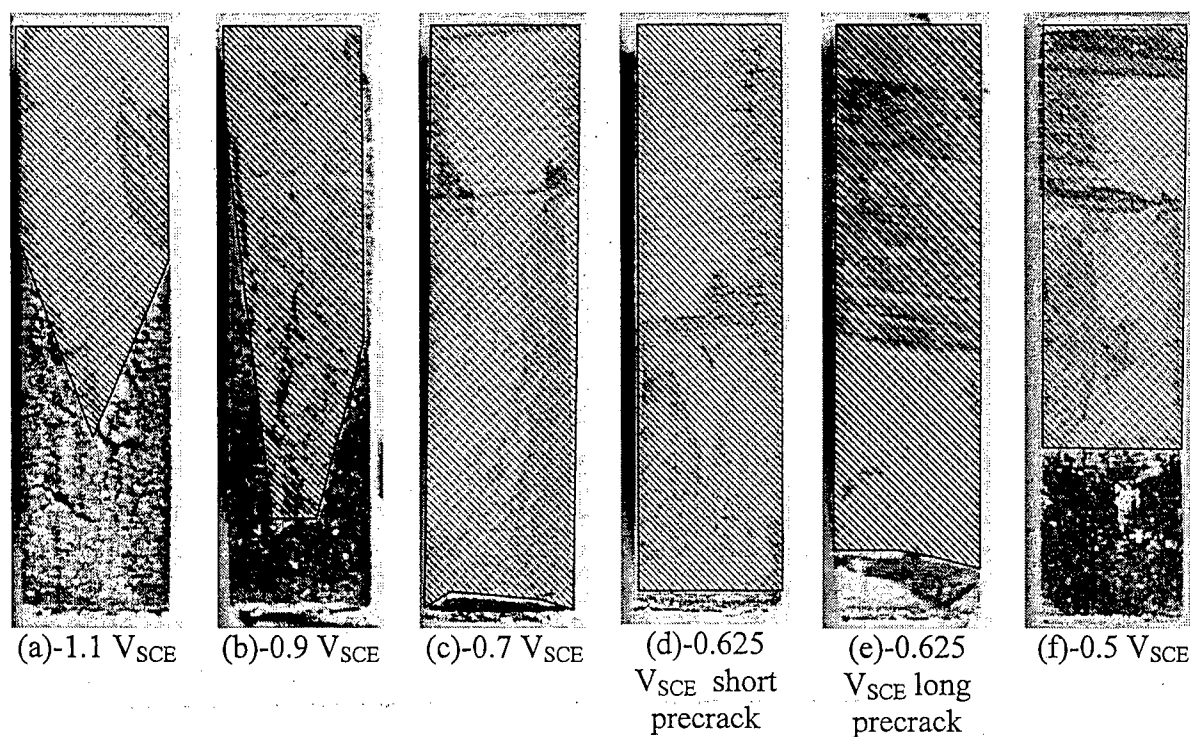


Figure 8 Low magnification optical images of the fracture surfaces for peak-aged AerMet™ 100 stressed at varying applied potentials in 3.5 % NaCl solution. All specimens measure 10 mm vertically in this view, with crack growth from bottom to top on the page. Parts (a) and (b) show significant crack growth at K below 20 MPa \sqrt{m} . (c) and (d) show no optically visible crack growth at $K = 50$ MPa \sqrt{m} . Specimen (e) with a larger precrack (0.76 mm) was loaded above $K = 100$ MPa \sqrt{m} , and still shows no visible crack. (f) Shows the fracture surface covered with black corrosion products.

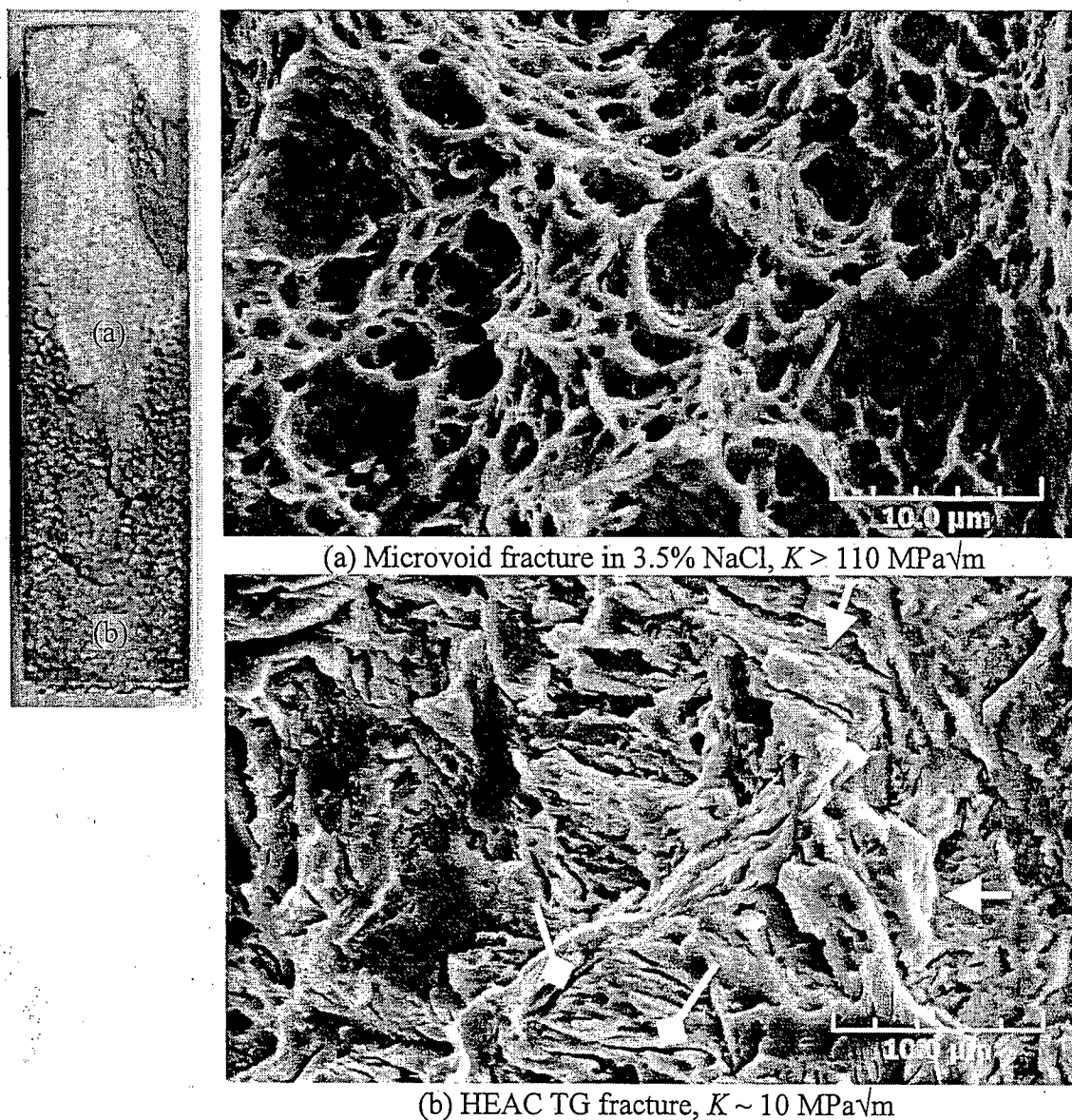


Figure 9 Scanning electron fractographs at two locations on the fracture surface of an AerMet™ 100 specimen fractured in 3.5 % NaCl polarized to $-1.100 \text{ V}_{\text{SCE}}$. The optical image locates the SEM images. (a) inside ductile fracture at $K > 110 \text{ MPa}\sqrt{\text{m}}$ showing microvoid fracture. (b) at crack initiation, triangular arrows showing possible martensite lath packet boundaries, and diamond tipped arrows showing possible martensite lath interface cracking.

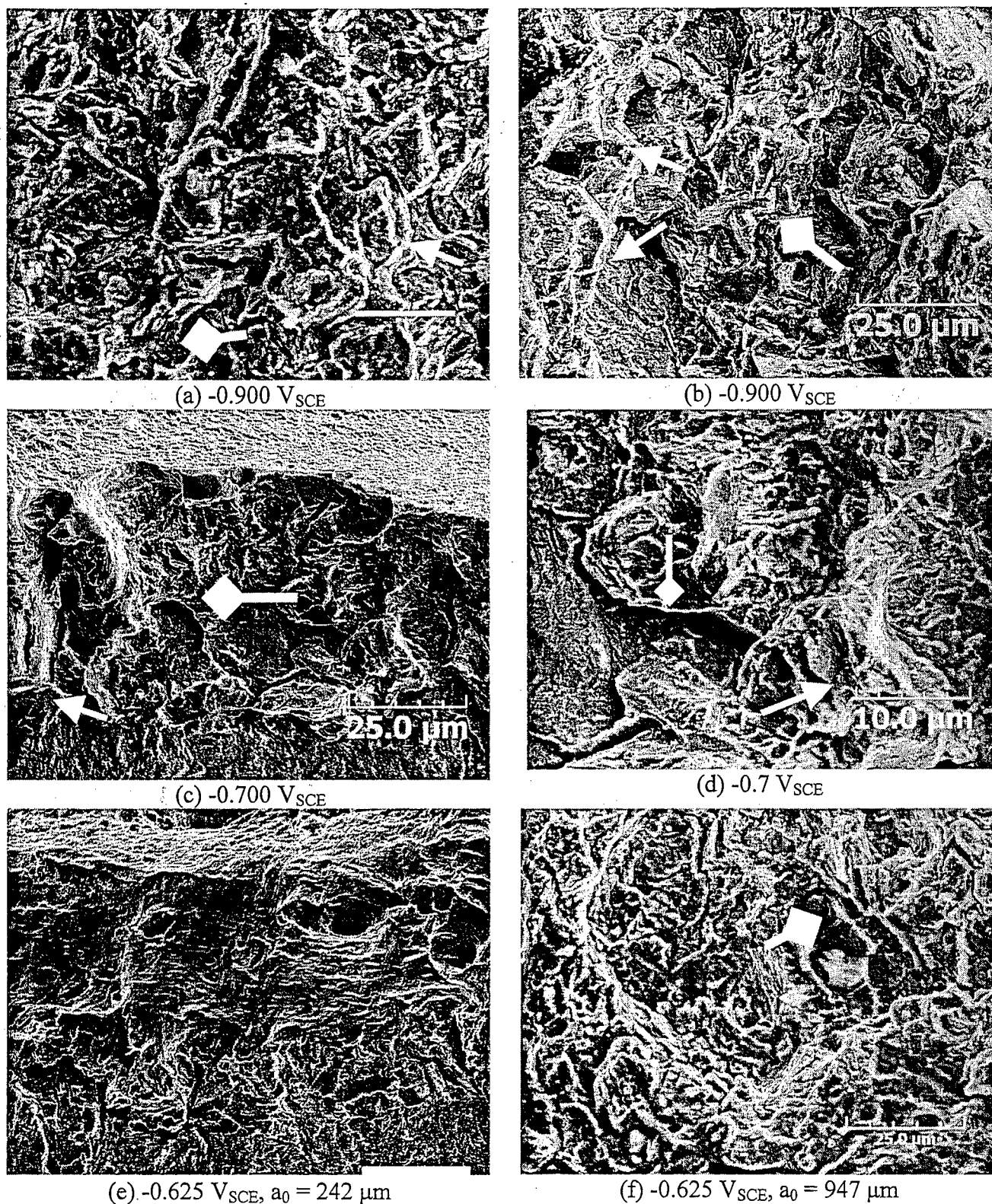


Figure 10 High resolution scanning electron images of fracture surfaces in peak-aged AerMet™ 100 in 3.5 % NaCl, showing the dependence of fracture mode on applied potential. All surfaces show predominantly transgranular fracture. (a) and (b) were both taken from the same specimen near the crack initiation adjacent to the fatigue precrack, but (b) shows limited IG fracture features. Triangular arrows show possible cracking at prior austenite grain boundaries or martensite lath packet boundaries, and diamond tipped arrows show possible martensite lath interface cracking. (d) shows some areas of an atypical flat fracture surface beyond TG HEAC, generally interpreted as stretch zones. All markers represent 25 μm except (d).

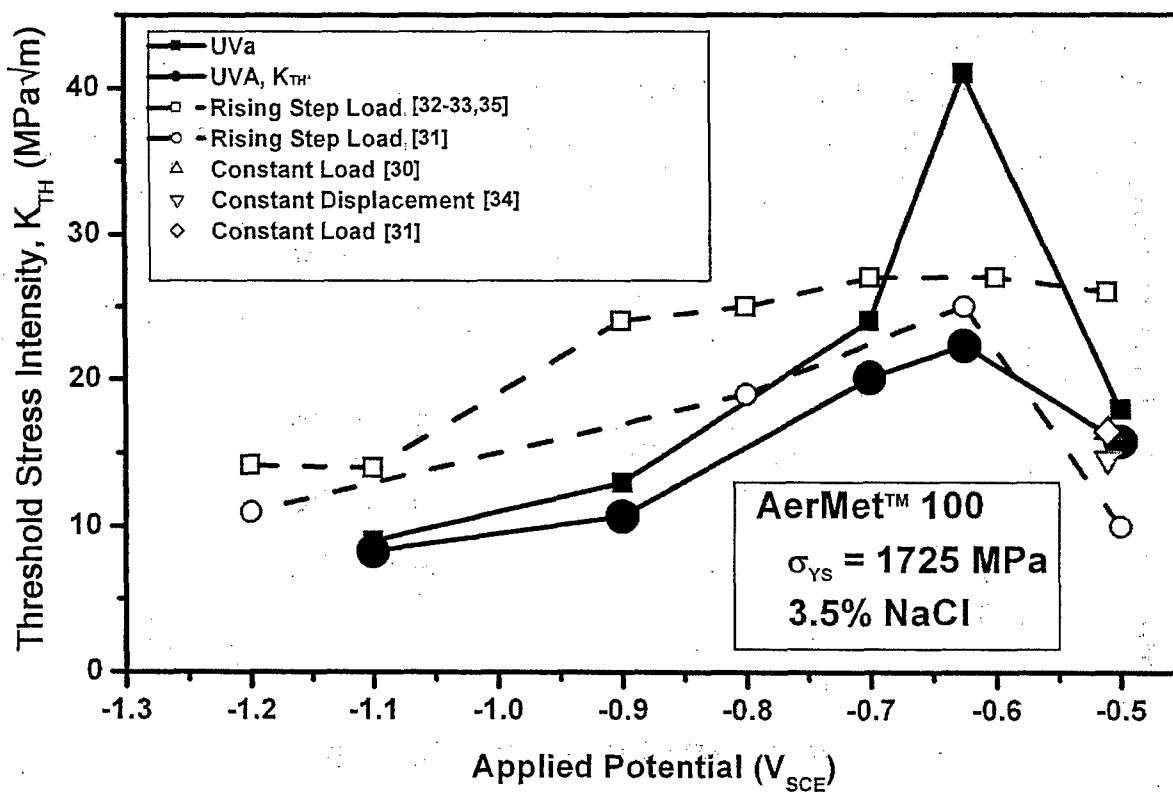


Figure 11 Threshold stress intensity vs. applied potential for peak-aged AerMet™ 100 in neutral 3.5% NaCl from various literature reports. K_{TH}^* , the level of K required to produce crack growth at da/dt of 1 nm/s, is also shown. The constant load-point displacement rate testing method can accurately replicate K_{TH} obtained from 10,000 h constant load tests.

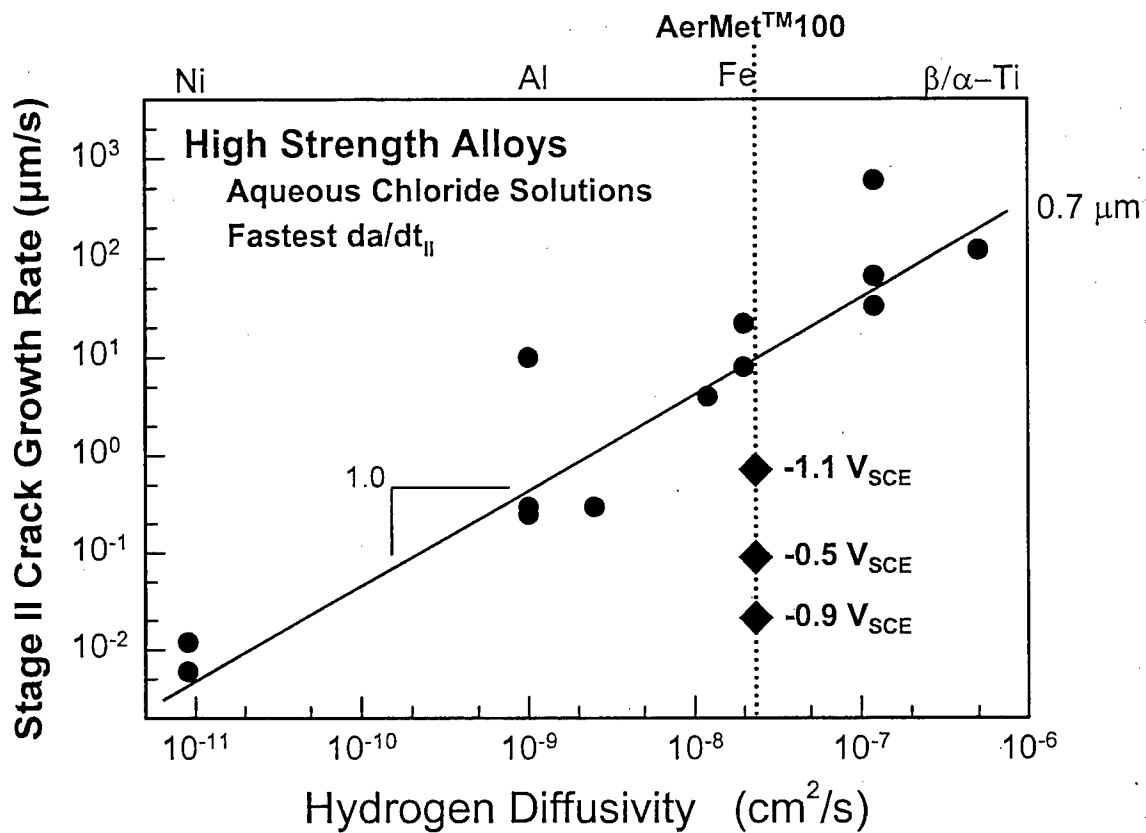


Figure 12 The dependence of the fastest-measured da/dt_{II} on D_H from permeation measurements for a variety of high strength alloys that exhibit HEAC in aqueous chloride solutions at 25°C .^[17]

References

1. N.V. Parthasaradhy: *Metal Finishing*, 1974, vol. May, pp. 88-94.
2. M.M. Markhlouf and Jr. Sisson, R.D.: *Hydrogen Effects on Material Behavior*, The Minerals, Metals & Materials Society, Worcester, MA, 1990, pp. 211-21,
3. T. Casanova, F. Soto, M. Eyraud and J. Crosier: *Corrosion Science*, 1997, vol. 39, pp. 529-37.
4. E.M.K. Hillier and M.J. Johnson: *Corrosion Science*, 2004, vol. 46, pp. 715-27.
5. R.A. Oriani and P.H. Josephic: *Acta Metallurgica*, 1977, vol. 25, pp. 979-88.
6. R.A. Oriani and P.H. Josephic: *Acta Metallurgica*, 1974, vol. 22, pp. 1065-74.
7. Richard P. Gangloff: *Environmentally Assisted Failure*, Elsevier Ltd., 2003, pp. 31-101,
8. C.J. McMahon Jr.: *Engineering Fracture Mechanics*, 2001, vol. 68, pp. 773-88.
9. M. Gao and R.P. Wei: *Met. Trans. A*, 1985, vol. 16A, pp. 2039-50.
10. S.P. Lynch: *Hydrogen Effects on Materials Behavior and Corrosion Deformation Interactions*, TMS, 2003, pp. 449-66,
11. C. D. Beachem: *Metallurgical Transactions*, 1972, vol. 3, pp. 437-51.
12. G.F. Li, R.G. Wu and T.C. Lei: *Metallurgical and Materials Transactions A*, 1992, vol. 23A, pp. 2879-85.
13. Y. Takeda and C.J. McMahon Jr.: *Met. Trans. A*, 1981, vol. 12A, pp. 1255-66.
14. J.P. Hirth: *Met. Trans. A*, 1980, vol. 11A, pp. 861-90.
15. N. Bandyopadhyay, J. Kameda and C.J. McMahon Jr.: *Met. Trans. A*, 1983, vol. 14A, pp. 881-8.
16. R.P. Gangloff and A. Turnbull: *Modeling Environmental Effects on Crack Initiation and Propagation*, TMS AIME, Warrendale, PA, 1986, pp. 55-81,
17. R. P. Gangloff: *Hydrogen Effects on Material Behavior and Corrosion Deformation Interactions*, The Minerals, Metals & Materials Society, Warrendale, PA, 2003, pp. 477-97,
18. Richard L.S. Thomas, John R. Scully and Richard P. Gangloff: *Met. Trans. A*, 2003, vol. 34A, pp. 327-44.
19. M.G.H. Wells: *Key Engineering Materials*, 1993, vol. 77-78, pp. 71-80.
20. G.B. Olson: *Advanced Materials and Processes*, 1997, vol. pp. 72-9.
21. R. Ayer and P.M. Machmeier: *Met. Trans. A*, 1993, vol. 24A, pp. 1943-55.
22. R. Ayer and P. M. Machmeier: *Metallurgical and Materials Transactions A*, 1996, vol. 27A, pp. 2510-17.

23. Choong Hwa Yoo, Hyuck Mo Lee, Jin W. Chan and J. W. Morris Jr.: *Metallurgical and Materials Transactions A*, 1996, vol. 27A, pp. 3466-72.
24. R. Ayer and P. M. Machmeier: *Metallurgical and Materials Transactions A*, 1998, vol. 29A, pp. 903-05.
25. J. Kozol and C. E. Neu: Report No. NAWCADWAR-92018-60, Naval Air Warfare Center, Warminster, PA, Jan 10, 1992 1992
26. P.F. Buckley, R. Brown, G.H. Graces, E.U. Lee, C.E. Neu and J. Kozol: *Metallic Materials for Lightweight Applications-Proceedings of the 40th Sagamore Army Materials Research Conference*, United States Army Laboratory Command, Watertown, MA, 1993, pp.
27. E.U. Lee: Report No. NAWCADWAR-94001-60, Naval Air Warfare Center, Warminster, PA, Oct. 23, 1993 1993
28. E.U. Lee: *Metallurgical and Materials Transactions A*, 1995, vol. 26A, pp. 1313-16.
29. A. Oehlert and A. Atrens: *Journal of Materials Science*, 1998, vol. 33, pp. 775-81.
30. E.U. Lee, H. Sanders and B. Sarkar: *Tri-Service Conference on Corrosion*, US Army Research Laboratory, 1999, pp.
31. Richard L.S. Thomas, Daoming Li, Richard P. Gangloff and John Scully: *Met. Trans. A*, 2002, vol. 33A, pp. 1991-2004.
32. Daoming Li, Richard P. Gangloff and John R. Scully: *Metallurgical and Materials Transactions A*, 2004, vol. 35A, pp. 849-64.
33. Joanne McLaughlin, John Douglas Weir and J. B. Boodey: *AEMR Conference*, 1998, pp.
34. R.W.J. Koers, A.H.M. Krom and A. Bakker: *Environmentally Assisted Cracking: Predictive Methods for Risk Assessment and Evaluation of Materials, Equipment, and Structures*, American Society for Testing and Materials, West Conshohocken, PA, 2000, pp. 303-16,
35. *2005 Annual Book of Astm Standards Vol. 3.01*, ASTM, West Conshohocken, PA, 2003, pp. 1004-15,
36. Wolfgang Dietzel: *Environmentally Assisted Cracking: Predictive Methods for Risk Assessment and Evaluation of Materials, Equipment, and Structures*, American Society for Testing and Materials, West Conshohocken, PA, 2000, pp. 317-26,
37. W. G. Clark and J.D. Landes: *Stress Corrosion-New Approaches, Astm Stp 610*, American Society for Testing and Materials, West Conshohocken, PA, 1976, pp. 108-27,
38. R.A. Oriani: *Fundamental Aspects of Stress Corrosion Cracking*, NACE, Houston, TX, 1969, pp. 32-50,
39. R.A. Oriani: *Acta Metallurgica*, 1970, vol. 18, pp. 147-57.
40. G.M. Pressouyre and I.M. Bernstein: *Met. Trans. A*, 1978, vol. 9A, pp. 1571-80.

41. S. Hinotani, Y. Ohmori and F. Terasaki: *Materials Science and Engineering*, 1985, vol. 76, pp. 57-69.
42. A. Turnbull, M.W. Carroll and D.H. Ferriss: *Acta Metallurgica*, 1989, vol. 37, pp. 2039-46.
43. B.G. Pound: *Hydrogen Effects on Material Behavior and Corrosion Deformation Interactions*, TMS, Warrendale, PA, 2003, pp. 93-103,
44. B.G. Pound: *Acta Metallurgica*, 1998, vol. 46, pp. 5733-43.
45. G. M. Pressouyre: *Acta Metallurgica*, 1980, vol. 28, pp. 895-911.
46. A. Turnbull: *Corrosion*, 2001, vol. 57, pp. 175-89.
47. B.F. Brown: *Stress Corrosion Cracking and Hydrogen Embrittlement of Iron Base Alloys*, National Association of Corrosion Engineers, Houston, TX, 1977, pp. 747-50,
48. D.P. Dautovich and S. Floreen: *Stress Corrosion Cracking and Hydrogen Embrittlement of Iron Base Alloys*, National Association of Corrosion Engineers, Houston, TX, 1977, pp. 798-815,
49. Brian E. Placzakis and J. H. Beatty: *Tri-Service Conference on Corrosion*, US Army Research Laboratory, Weapons and Materials Research Directorate, 1997, pp. 7.18-7.32,
50. J.R. Scully, Beth. A. Kehler, Yongwon Lee and R.P. Gangloff: *Tri-Service Corrosion Conference*, NACE, Orlando, Florida, 2005, pp.
51. M.A. Jakab and J.R. Scully: *Nature Materials*, 2005, vol. 4, pp. 667-70.
52. B.G. Ateya and H.W. Pickering: *Journal of the Electrochemical Society*, 1975, vol. 122, pp. 1018-26.
53. H.W. Pickering: *Corrosion Science*, 1989, vol. 29, pp. 325-41.
54. James M. Dahl: *Advanced Materials & Processes*, 2000, vol. May, pp. 33-.
55. H.H. Johnson: *Materials Research & Standards*, 1965, vol. 5, pp. 442-45.
56. Richard P. Gangloff, Donald C. Slavik, Robert S. Piascik and Robert H. Van Stone: *Small-Crack Test Methods, Astm Stp 1149*, American Society for Testing and Materials, Philadelphia, 1992, pp. 116-68,
57. Robert S. Piascik and Richard P. Gangloff: *Met. Trans. A*, 1991, vol. 22A, pp. 2415-28.
58. M.J. Haynes and R.P. Gangloff: *Journal of Testing and Evaluation*, 1997, vol. 25, pp. 82-98.
59. H. Tada, P. C. Paris and G. R. Irwin: *The Stress Analysis of Cracks Handbook*, Paris Productions Incorporated, St. Louis, Missouri, 1985, pp.
60. R.L.S. Thomas: University of Virginia, unpublished research, 1999
61. B. Force and H.W. Pickering: *Journal of Materials*, 1995, vol. 47, pp. 22-27.

62. P.K. Subramanyan: *Comprehensive Treatise of Electrochemistry Volume 4: Electrochemical Materials Science*, Plenum Press, New York, NY, 1981, pp. 411-62.
63. A. Turnbull, D. H. Ferriss and H. Anzai: *Mater. Sci. Engr. A*, 1996, vol. 206, pp. 1-13.
64. K.N. Akhurst and T.J. Baker: *Met. Trans. A*, 1981, vol. 12A, pp. 1059-70.
65. Yueguang Wei and J.W. Hutchinson: *Journal of Mechanics and Physics of Solids*, 1997, vol. 45, pp. 1253-73.
66. H. Jiang, Y. Huang, Z. Zhuang and K.C. Hwang: *Journal of Mechanics and Physics of Solids*, 2001, vol. 49, pp. 979-93.
67. Z. Gao and J. W. Morris Jr.: *Scripta Metallurgica*, 2005, vol. 53, pp. 933-36.
68. Y. H. Kim, H. J. Kim and J. W. Morris Jr.: *Metallurgical and Materials Transactions A*, 1986, vol. 17A, pp. 1157-64.
69. R.O. Ritchie, V.F. Castro Cedeno, V.F. Zackay and E.R. Parker: *Met. Trans. A*, 1978, vol. 9A, pp. 35-40.
70. G.B. Olson: *Innovations in Ultrahigh Strength Steel Technology, 34th Sagamore Army Materials Research Conference*, US Army Laboratory Command, Watertown, MA, 1987, pp. 3-66,
71. J. I. Kim and J. W. Morris Jr.: *Metallurgical and Materials Transactions A*, 1980, vol. 12A, pp. 1957-63.
72. A. Szummer: *Hydrogen Degradation of Ferrous Alloys*, Noyes Publications, Park Ridge, NJ, 1985, pp.
73. M. L. Holzworth and M. R. Louthan Jr.: *Corrosion*, 1968, vol. 24, pp. 110-24.
74. G.M. Pressouyre: *Hydrogen Effects in Metals*, The Minerals, Metals, and Materials Society, Warrendale, PA, 1981, pp. 27-36,
75. T.Y. Zhang, H. Sheu and J.E. Hack: *Scripta metall. Mater.*, 1992, vol. 27, pp. 1605.
76. T.Y. Zhang and J.E. Hack: *Metallurgical and Materials Transactions A*, 1999, vol. 30A, pp. 155.
77. W.W. Gerberich, T. Livne and X. Chen: *Modeling Environmental Effects on Crack Growth Processes*, The Metallurgical Society, Warrendale, PA, 1985, pp.
78. J. Toribio and V. Kharin: *International Journal of Fracture*, 1997, vol. 88, pp. 233-45.
79. P. Shewmon: The Minerals, Metals, & Materials Society, Warrendale, PA, 1989, pp. 9-51,
80. P. Doig and G. T. Jones: *Metallurgical and Materials Transactions A*, 1977, vol. 8A, pp. 1993-98.
81. W.W. Gerberich, T. Livne, X.-F. Chen and M. Kaczorowski: *Met. Trans. A*, 1988, vol. 19A, pp. 1319-34.

82. M.M. Hall and D.M. Symons: *Chemistry and Electrochemistry of Stress Corrosion Cracking*, The Minerals, Metals, & Materials Society, Warrendale, PA, 2001, pp. 447-66,
83. Y. Katz, N. Tymiak and W. W. Gerberich: *Engineering Fracture Mechanics*, 2001, vol. 68, pp. 619-46.
84. W. W. Gerberich, P.G. Marsh and J.W. Hoehn: *Hydrogen Effects in Metals*, TMS, Warrendale, PA, 1996, pp. 539-,
85. A.J. Kumnick and H.H. Johnson: *Metallurgical Transactions*, 1974, vol. 5, pp. 1199-206.
86. I.W. Kang, S.I. Pyun and K.T. Kim: *Scripta Metallurgica*, 1989, vol. 23, pp. 223-6.
87. R.A. Page and W.W. Gerberich, The effect of hydrogen source on crack initiation in 4340 steel. *Metall. Trans. A*, 13A, 1982, 305-311.
88. R.P. Gangloff and R.P. Wei: *Small Fatigue Cracks*, R.O. Ritchie and J. Lankford, eds., TMS-AIME, Warrendale, PA., 1986, pp. 239-264.
89. B.P. Somerday, L.M. Young and R.P. Gangloff: *Fatigue and Fracture of Engineering Materials and Structures*, 2000, Vol. 23, pp. 39-58.
90. R.P. Gangloff and R.P. Wei: *Fractography in Failure Analysis*, ASTM STP 645, ASTM, Philadelphia, PA, 1978, pp. 87-106.
91. B.A. Kehler, Yongwon Lee, J.R. Scully and R.P. Gangloff: University of Virginia, unpublished research, 2004.
92. R.P. Wei and R.P. Gangloff: *Fracture Mechanics: Perspectives and Directions*, ASTM STP 1020, R.P. Wei and R.P. Gangloff, eds., ASTM, Philadelphia, PA, 1989, pp. 233-264.
93. D.M. Symons: *Engineering Fracture Mechanics*, 2001, vol. 68, pp. 751-71.
94. J.R. Scully and R.P. Gangloff, "Mechanism-Based Modeling of Hydrogen Assisted Cracking in High Strength Alloys for Marine Applications", SEAS Proposal No. MSE-DOD/ONR-2792-06, University of Virginia, Charlottesville, VA (2006).